Yield surface for void growth and coalescence of porous anisotropic materials under axisymmetric loading

Cedric Senac, Jeremy Hure, Benoît Tanguy

To cite this version:

Cedric Senac, Jeremy Hure, Benoît Tanguy. Yield surface for void growth and coalescence of porous anisotropic materials under axisymmetric loading. Journal of the Mechanics and Physics of Solids, 2023, 179, pp.105365. ⟨10.1016/j.jmps.2023.105365⟩. ⟨cea-04541184⟩

HAL Id: cea-04541184

https://cea.hal.science/cea-04541184v1

Submitted on 1 Oct 2025

Yield surface for void growth and coalescence of porous anisotropic materials under axisymmetric loading

C. Sénac[a,*], J. Hure[a], B. Tanguy[a]

[a] *Université Paris-Saclay, CEA, Service d'Étude des Matériaux Irradiés, 91191, Gif-sur-Yvette, France*

Abstract

Ductile fracture in metallic alloys occurs by growth and coalescence of cavities. Growth, also referred to as homogeneous yielding, refers to rather diffuse plasticity around cavities, while coalescence, also termed as inhomogenous yielding, corresponds to the localization of plasticity along some planes or directions. Coalescence can develop in various patterns; three coalescence modes have been observed experimentally: internal necking, coalescence in columns and void sheeting. Plastic anisotropy of the material is known to have a significant effect on both homogeneous and inhomogeneous yielding. Therefore, in the present study, yield criteria accounting for the transition from homogeneous yielding to inhomogeneous yielding modes in anisotropic porous materials are obtained using kinematic limit analysis on a cylindrical unit-cell with a coaxial cylindrical cavity. Two types of plastic anisotropy are considered: Hill (1948) plasticity and crystal plasticity. The proposed analytical yield criteria are compared to numerical limit analysis computations and are found to qualitatively agree with simulations. In particular, plastic anisotropy, void shape effects and their coupling are well captured, especially regarding yield stresses and deformation modes. Finally, an homogenized model for Hill porous materials is obtained by supplementing evolution laws for microstructural parameters (void aspect ratio and ligament size ratios) derived from sequential limit analysis. Proposed evolution laws are then discussed in the light of numerical results and experimental evidence.

Keywords: Ductile fracture, Porous materials, Necklace coalescence, Internal necking, Strain localization, Hill plasticity, Crystal plasticity

1. Introduction

It has been known for decades that the process of ductile fracture in most metallic alloys happens through growth and coalescence of cavities originating from inclusions (*e.g.* Benzerga and Leblond (2010); Pineau et al. (2016)). On the one hand, void growth manifests as a rather homogeneous yielding of the material, with diffuse plasticity at the scale of cavities. On the other hand, void coalescence arises from the inhomogeneous distribution of the plastic flow: due to strong interactions between cavities, strain localizes in specific zones linking voids. Following the seminal contributions of Rice and Tracey (1969) and Gurson (1977), homogeneous yielding in porous materials (Fig. 1a) has been thoroughly studied: for isotropic materials, yield criteria for spherical voids (Gurson, 1977), spheroidal voids (Gologanu and Leblond, 1997) and ellipsoidal voids (Madou and Leblond, 2012a) have been proposed. These criteria were extended to anisotropic materials through Hill (1948) plasticity, respectively in Benzerga and Besson (2001), Monchiet et al. (2008), Keralavarma and Benzerga (2010) and Morin et al. (2015b), and to porous single crystals by Han et al. (2013), Paux et al. (2015) and Mbiakop et al. (2015). Thus, further improvements of the prediction of yield criteria for porous materials lie in the accurate modeling of inhomogeneous yielding and the transition from homogeneous yielding to inhomogeneous yielding.

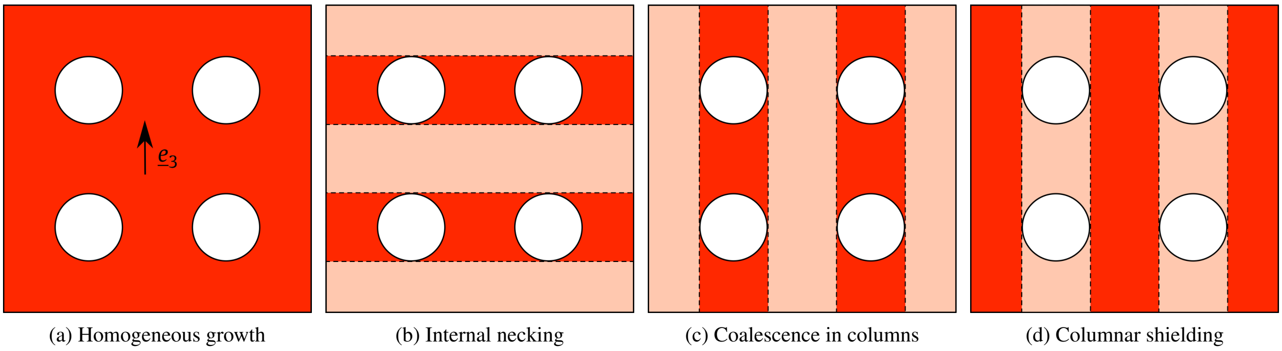

(a) Homogeneous growth (b) Internal necking (c) Coalescence in columns (d) Columnar shielding

Figure 1: Possible modes of yielding of a periodic array of voids subjected to an axisymmetric loading of principal axis $\underline{e}_3$.

Inhomogeneous yielding in porous materials has been modeled more recently than homogeneous yielding. Experimental observations of coalescence reveal various possible types of interactions between cavities (Benzerga et al., 2004a).

---

[*] Corresponding author: cedric.senac@polytechnique.org

Internal necking and necklace coalescence are the most commonly observed coalescence modes. The former, where localization occurs mostly perpendicular to the main loading direction, is alternatively referred to as coalescence in layers (Fig. 1b), while in the latter, also denoted as coalescence in columns, localization happens along the main loading direction (Fig. 1c). In a major contribution, Thomason (1985) used limit-analysis to derive a coalescence stress for internal necking later employed as a yield criterion. Thomason's yield criterion was used and improved by a certain number of studies (Pardoen and Hutchinson, 2000; Benzerga, 2002; Benzerga et al., 2004b) or specialized to anisotropic materials (Yerra et al., 2010) until analytical expressions were finally obtained by Benzerga and Leblond (2014), Morin et al. (2015a) (cylindrical voids), Hure and Barrioz (2016) (flat cylindrical voids) and Barrioz et al. (2018) (elliptic-cylindrical voids). Shear-assisted coalescence has been incorporated in the model by Tekoğlu et al. (2012), Torki et al. (2015) and Torki et al. (2017). These inhomogeneous yield criteria have been combined to homogeneous yield criteria using multi-surface plasticity framework (Benzerga and Leblond, 2010; Keralavarma, 2017; Torki et al., 2021). Another approach has been proposed recently consisting of deriving a single yield criterion able to represent both homogeneous and inhomogeneous yielding using limit-analysis with suitable velocity fields (Morin et al., 2016a; Torki, 2019). All these advances have focused on coalescence in layers; nonetheless, necklace coalescence is important in the prediction of ductile fracture of many materials, as will be shown below.

From an experimental perspective, the historical observations of coalescence in columns (Cheremskoy et al., 1990; Pardoen, 1998; Benzerga, 2000) were scarce, which has led to a false sentiment that this deformation mode was anecdotal and could be neglected. The paucity of experimental evidence was explained by the fact that coalescence in columns usually cannot be identified on fracture surfaces — contrary to shear-assisted coalescence and internal necking — and must therefore be glimpsed through metallographic examinations of areas away from fracture surfaces or on samples subjected to interrupted mechanical tests. The recent development of X-ray tomography has revealed that this phenomenon is in fact more common (Fig. 2a) (Requena et al., 2014; Seo et al., 2015; Guo et al., 2020). Observations of necklace coalescence, originally limited to steels (Cheremskoy et al., 1990; Benzerga, 2000) and copper (Pardoen, 1998) with strings of second-phase particles caused by metal forming and oriented along the loading direction, were also diversified to other materials. In pure tantalum with equiaxed grains, coalescence in columns was shown to be dominant (Boyce et al., 2013), underlying that a specific distribution of inclusions is not a prerequisite to observe this phenomenon (Fig. 2b). Furthermore, it was seen that necklace coalescence can give birth to micro-cracks (Fig. 2c) in annealed bainitic steels (Saeidi et al., 2015). Outside of metallic materials, intense coalescence in columns was unambiguously identified during fracture of aged polyethylene films in which void nucleation at the amorphous phase was enabled by chemical micro-cracks (Rodriguez et al., 2020). When coalescence in columns is significant, it has an influence on the fracture process and the ductility of the material, although its effect is eminently ubiquitous. On the one hand, fracture strain can be reduced if the final crack originates from a necklace coalescence micro-crack (Saeidi et al., 2015), if internal necking occurs between voids formed through necklace coalescence (Requena et al., 2014) or if a shear instability is fostered by elongated coalesced cavities (Rodriguez et al., 2020). On the other hand, coalescence in columns can be responsible for delaminations (Benzerga and Leblond, 2010) that lower the stress triaxiality, making crack propagation perpendicularly to the loading direction more difficult (Bramfitt and Marder, 1977; Pala and Dzioba, 2018; Wang et al., 2022), which can result in an increase of the fracture strain. For instance, coalescence in columns seems partially responsible for the observed ductility of pure tantalum (Boyce et al., 2013).

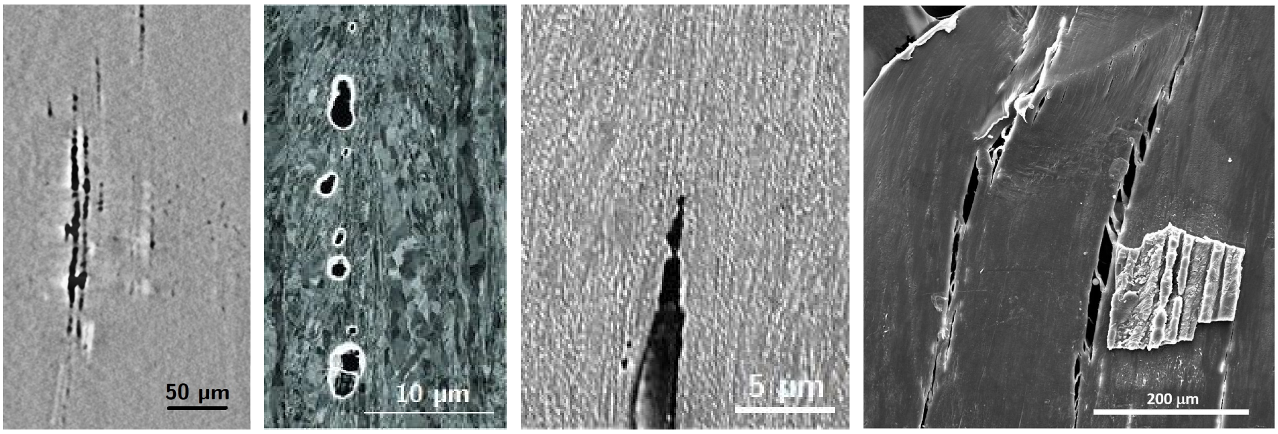

(a) (b) (c) (d)

Figure 2: Experimental evidence of necklace coalescence in various materials: (a) dual-phase steel (Requena et al., 2014); (b) pure tantalum (Boyce et al., 2013); (c) upper bainitic steel (Saeidi et al., 2015); (d) UV-aged low-density polyethylene (Rodriguez et al., 2020). The applied loading was vertical in all cases; however, note that specimen (d) has rotated a little following fracture.

From a numerical perspective, porous plasticity models that do not incorporate coalescence in columns display discrepancies when compared to numerical results with general boundary conditions, as seen in Chouksey et al. (2019). Another localization mode, in which the central column of the unit-cell is shielded from plasticity — referred to as *columnar shielding* in the following — was also reported multiple times in unit-cell simulations (Chouksey et al., 2019, 2020; Chouksey and Basu, 2021). An earlier model of coalescence in columns was provided by Gologanu et al. (2001) on a cylindrical unit-cell: the central column was modeled as a homogeneous porous material experiencing void growth, while the outer hollow cylinder followed plastic incompressibility laws. However, the approximate nature of implicit velocity fields considered in this model had detrimental effects on the micromechanics of coalescence (Torki et al., 2023). Recently, explicit limit-analysis of coalescence in columns and columnar shielding was performed by Torki et al. (2023) for an isotropic von Mises matrix; their results confirmed that accounting for these additional localization modes allowed for a better prediction of yield surfaces provided by unit-cell simulations.

It is known from experiments (Benzerga et al., 2004a; Benzerga and Leblond, 2010), theory (Keralavarma and Chockalingam, 2016; Hure, 2019) and simulations (Keralavarma et al., 2011; Yerra et al., 2010; Ling et al., 2016; Sénac et al., 2022) that plastic anisotropy has a strong influence on material ductility, through significant effects on both homogeneous and inhomogeneous yielding. Since metal forging and forming are known to induce strong anisotropy in metallic components, it means that specific yield surfaces for porous materials exhibiting plastic anisotropy are needed. As stated before, numerous studies have been carried out on the homogeneous yielding of anisotropic materials. Criteria for internal necking have also been established in Hill materials (Keralavarma and Chockalingam, 2016) and single crystals (Hure, 2019). Therefore, the goal set to the present study is to develop a yield criterion for both Hill materials and single crystals that would account for homogeneous yielding (Fig. 1a), inhomogeneous yielding (Fig. 1b,c,d), and the transition from one mode to another, for axisymmetric loading conditions.

The paper is divided in three main parts. In the first part, a multi-surface yield criterion for anisotropic porous materials following Hill's criterion is developed; this model is relevant for polycrystalline materials where voids are significantly larger than the grain size. It is derived through limit-analysis of two velocity fields: a field accounting for the transition from homogeneous yielding (Fig. 1a) to coalescence in columns (Fig. 1c,d), as in Torki et al. (2023), and a field accounting for the transition from homogeneous yielding to internal necking (Fig. 1b), as in Morin et al. (2016a). Subsequently, the final criterion is checked against unit-cell simulations. Since this first model cannot be applied to alloys in which voids are smaller than the grain size, a yield surface for porous single crystals is developed in a second part. It is obtained using an approximate method relying on average Taylor factors and compared to numerical yield surfaces. In a third part, a complete homogenized model is obtained for Hill materials by supplementing the multi-surface yield criterion with microstructure evolution laws derived from sequential limit-analysis. Finally, the model is discussed in the light of numerical velocity fields and ductile fracture experimental evidence.

2. Problem statement

In the following, vectors are shown as $\underline{a}$ of norm a, second-order tensors as $\boldsymbol{a}$ and fourth-order tensors as $\mathbb{A}$. Einstein summation convention is used on Latin indices but not Greek ones.

2.1. Porous material description

In this study, a porous material is considered with an homogeneous matrix where cavities of identical size and shape are embedded. As a first approximation, cavities are supposed to be spheroidal of aspect ratio w and the real distribution of voids is modeled as a periodic array of hexagonal lattice, with the void main axis and the lattice main axis being along $\underline{e}_3$ (Fig. 3a).

The above-defined material is subjected to axisymmetric boundary conditions. An approximation of this material is provided by a cylindrical unit-cell Ω of main axis along $\underline{e}_3$, as shown on Fig. 3b. The unit cell half-height is called H and its radius R; it contains a coaxial cylindrical void ω and is characterized by three dimensionless ratios:

$$\chi = \frac{r}{R} \quad , \quad c = \frac{h}{H} \quad , \quad w = \frac{h}{r} \tag{1}$$

χ is the transverse ligament size ratio, c is the axial ligament size ratio and w is the void aspect ratio. If $w > 1$, the void is prolate, and $w < 1$ means that the void is oblate. This approximated unit-cell is loaded axisymetrically with the following velocity boundary conditions:

$$v_\rho(R, z) = R D_{\rho\rho} \quad , \quad v_z(\rho, \pm H) = \pm H D_{33} \tag{2}$$

with $\boldsymbol{D}$ the (volume-averaged) macroscopic strain rate tensor. As discussed in Benzerga and Leblond (2014) and later shown in Morin et al. (2016a), these boundary conditions allow to consider both homogeneous and inhomogeneous yielding. The microscopic Cauchy stress tensor is referred to as $\boldsymbol{\sigma}$ and the macroscopic one as $\boldsymbol{\Sigma}$, these tensors being related by $\boldsymbol{\Sigma} = \int_\Omega \boldsymbol{\sigma} / |\Omega|$.

2.2. Kinematic limit analysis

In this work, the plastic yielding of the approximated unit-cell is studied using kinematic limit analysis (Suquet, 1982). Limit analysis relies on finding a (trial) velocity field that is both incompressible and compatible with boundary conditions. This trial velocity field is then used to estimate the yield surface (Benzerga and Leblond, 2010). The set of trial velocity fields $\underline{v}$ that satisfy boundary conditions (Eq. 2) as well as matrix incompressibility $\mathrm{tr}\,(\dot{\boldsymbol{\varepsilon}}) = 0$ is denoted $\mathcal{K}\,(\boldsymbol{D})$. The microscopic plastic dissipation of such a velocity field is:

$$\varpi\left(\underline{v}\left(\underline{x}\right)\right) \equiv \sup_{\boldsymbol{\sigma}^* \in \mathscr{C}} \left(\boldsymbol{\sigma}^* : \boldsymbol{d}\left(\underline{x}\right)\right) \tag{3}$$

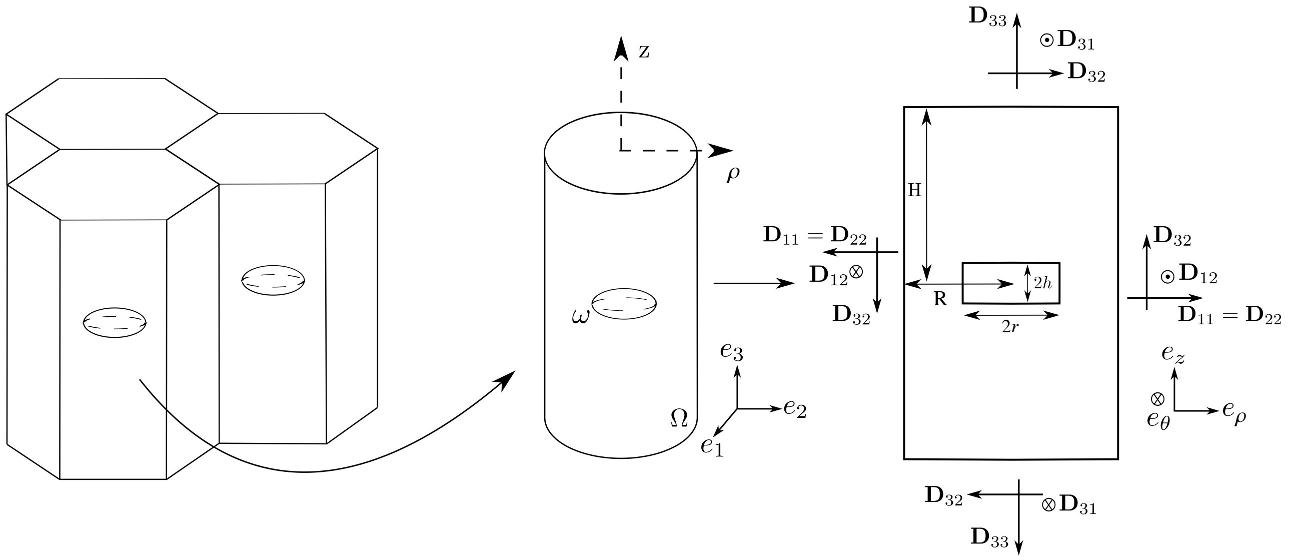

(a)

(b)

Figure 3: Cylindrical unit-cell considered as an approximation of a unit-cell of a periodic array of voids of hexagonal lattice under periodic boundary conditions.

where $\boldsymbol{d}$ is the strain rate field deriving from $\underline{v}$ and $\mathscr{C}$ is the microscopic elasticity domain of the matrix. Each element $\underline{v} \in \mathcal{K}(\boldsymbol{D})$ provides an upper bound Π_+ for the macroscopic dissipation Π, defined as:

$$\Pi(\boldsymbol{D}) = \inf_{\underline{v}\in\mathcal{K}(\boldsymbol{D})} \frac{1}{|\Omega|}\int_{\Omega} \varpi\left(\underline{v}\left(\underline{x}\right)\right) \tag{4}$$

If the velocity field exhibit a discontinuity $\Delta\underline{v} = \left|\Delta\underline{v}\right|\underline{t}$ on a given surface $\mathcal{S}_d$ of normal $\underline{n}$ ($\underline{t}$ and $\underline{n}$ are unit vectors), an additional dissipation term has to be added to the dissipation upper-bound Π_+ (Salençon, 1983):

$$\Pi_+^{\mathrm{surf}}(\boldsymbol{D}) = \frac{1}{|\Omega|}\int_{\mathcal{S}_d} \left|\Delta\underline{v}\right| \sup_{\boldsymbol{\sigma}^*\in\mathscr{C}} \left(\boldsymbol{\sigma}^* : \boldsymbol{d}^{(\mathrm{I})}\right) \quad \text{with} \quad \boldsymbol{d}^{(\mathrm{I})} = \frac{1}{2}\left(\underline{t}\otimes\underline{n} + \underline{n}\otimes\underline{t}\right) \tag{5}$$

Hill-Mandel lemma (*e.g.* Nemat-Nasser and Hori (1993)) along with Eqs. 3, 4 allows to write that:

$$\forall\boldsymbol{D}\,,\quad \boldsymbol{\Sigma} : \boldsymbol{D} \leq \Pi\left(\boldsymbol{D}\right) \tag{6}$$

which is used to assess the yield surface. Indeed, the yield surface of the material is the boundary of the elasticity domain described by Eq. 6. This means that for each $\boldsymbol{\Sigma}$ on the yield surface, there is a strain rate $\boldsymbol{D}$ for which $\boldsymbol{\Sigma} : \boldsymbol{D} = \Pi\left(\boldsymbol{D}\right)$. Thus, the hyperplane $\boldsymbol{\Sigma} : \boldsymbol{D}$ must be tangent to surface $\Pi(\boldsymbol{D})$. On the one hand, if Π is differentiable at the point $\boldsymbol{D}_0$ where multi-dimensional tangency occur, then tangency implies that:

$$\boldsymbol{\Sigma} : \boldsymbol{D}_0 = \Pi(\boldsymbol{D}_0)\,,\quad \boldsymbol{\Sigma} = \frac{\partial\Pi}{\partial\boldsymbol{D}}(\boldsymbol{D}_0) \tag{7}$$

On the other hand, if Π is not differentiable, then multi-dimensional tangency become:

$$\boldsymbol{\Sigma} : \boldsymbol{D}_0 = \Pi(\boldsymbol{D}_0)\,,\quad \boldsymbol{\Sigma} \in \partial\Pi(\boldsymbol{D}_0) \tag{8}$$

with $\partial\Pi(\boldsymbol{D}_0)$ denoting the subdifferential of Π at point $\boldsymbol{D}_0$, *i.e.* the set of subgradients $\boldsymbol{S}$ such that

$$\Pi(\boldsymbol{D}) - \Pi(\boldsymbol{D}_0) \geq \boldsymbol{S} : (\boldsymbol{D} - \boldsymbol{D}_0) \tag{9}$$

For each trial velocity field, Eq. 7_b (or Eq. 8_b) provides an upper-bound Π_+ of the macroscopic dissipation Π and thus an upper-bound of the yield surface. In the following, for each trial field, the corresponding Π_+ and its subsequent upper-bounds will still be denoted Π for convenience.

3. Yield surface for porous Hill materials

In the first part, plastic anisotropy will be modeled by the well-known Hill plasticity (Hill, 1948). The matrix material is supposed to be elasto-plastic, obeying associated Hill criterion:

$$\mathcal{F}\left(\boldsymbol{\sigma}\right) = \left(\frac{\sigma_{\mathrm{eq}}^{\mathrm{H}}}{\sigma_0}\right)^2 - 1 = \frac{3}{2}\frac{\boldsymbol{\sigma} : \mathbb{h} : \boldsymbol{\sigma}}{\sigma_0^2} - 1 \tag{10}$$

with $\mathbb{h}$ the Hill stress anisotropy tensor and σ_0 the uniaxial yield strength in a given direction. The matrix material is incompressible, thus $\mathbb{J} : \mathbb{h} = \mathbb{h} : \mathbb{J} = 0$ with $\mathbb{J} = \frac{1}{3}\boldsymbol{I} \otimes \boldsymbol{I}$. The associated equivalent strain rate is $d_{\text{eq}} = \sqrt{\frac{2}{3}\boldsymbol{d} : \hat{\mathbb{h}} : \boldsymbol{d}}$ with $\hat{\mathbb{h}}$ a tensor verifying $\hat{\mathbb{h}} : \mathbb{h} = \mathbb{h} : \hat{\mathbb{h}} = \mathbb{K}$, where $\mathbb{K} = \mathbb{I} - \mathbb{J}$. In a base of orthotropy, the components of $\hat{\mathbb{h}}$ can be obtained from the components of $\mathbb{h}$ following the formulas given in Morin (2012). More fundamentally, $\hat{\mathbb{h}}$ is linked to $\mathbb{h}$ through linear algebra, as shown in Sénac et al. (2023). Microscopic plastic dissipation (Eq. 3) writes:

$$\sup_{\boldsymbol{\sigma}^* \in \mathscr{C}} (\boldsymbol{\sigma}^* : \boldsymbol{d}) = \sigma_0 d_{\text{eq}} \tag{11}$$

The yield surface for porous Hill materials under axisymmetric loading will be obtained through the conjunction of a yield criterion describing the gradual localization of strain in vertical zones (Section 3.1) and a yield criterion describing the gradual localization of strain in horizontal layers (Section 3.2).

3.1. From homogeneous yielding to inhomogeneous yielding in columns

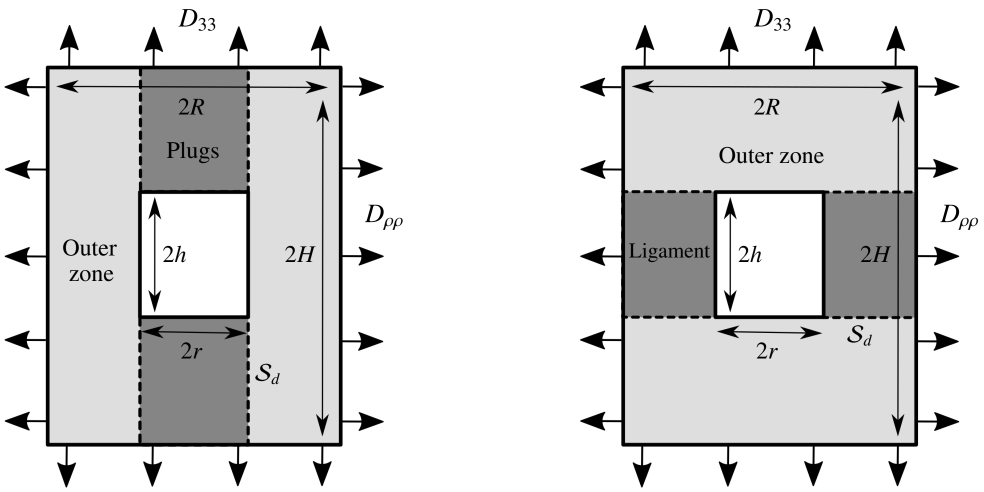

(a) Columnar localization

(b) Layered localization

Figure 4: Geometry of the zones used to define trial velocity fields kinematically admissible with the boundary conditions.

In this section, the transition from homogeneous yielding (Fig. 1a) to columnar localization, which can manifest either as columnar shielding (Fig. 1c) or as coalescence in columns (Fig. 1d) is considered to obtain the related yield criterion. This yield criterion is therefore an extension of the criterion developed by Torki et al. (2023) to anisotropic materials following Hill's criterion (Eq. 10).

3.1.1. Trial velocity field and associated dissipation

The trial velocity field proposed in Torki et al. (2023) is used to account for the situation depicted in Fig. 1a,c,d and is defined in the geometry shown in Fig. 4a:

$$\begin{array}{lll} \text{Outer zone:} & v_\rho^{(M)}(\rho) = \dfrac{1}{2}\left(\dfrac{R^2}{\rho}D_{kk} - \rho D_{33}\right), & v_z^{(M)}(z) = zD_{33} \\ \text{Plugs:} & v_\rho^{(P)}(\rho) = \dfrac{1}{2}\left(\dfrac{\rho}{\chi^2}D_{kk} - \rho D_{33}\right), & v_z^{(P)}(z) = \dfrac{H-z}{\chi^2}D_{kk} + zD_{33} \end{array} \tag{12}$$

This trial velocity field is incompressible, kinematically admissible with Eq. 2 and displays a purely tangential discontinuity along $\mathcal{S}_d$ $(\rho = r)$. As this field has been shown in Torki et al. (2023) to lead to results in good agreement with numerical simulations for isotropic materials, it will be adopted to study general anisotropic materials. Then, the macroscopic plastic dissipation is the sum of volume terms corresponding to the plugs (P) and the outer zone (O), as well as a surface term originating from the velocity tangential discontinuity at the interface between zones P and O:

$$\Pi(\boldsymbol{D}) = \underbrace{\frac{1}{|\Omega|}\int_{\Omega_P} \sigma_0 d_{\text{eq}}^{(P)}}_{\Pi^{(P)}} + \underbrace{\frac{1}{|\Omega|}\int_{\Omega_O} \sigma_0 d_{\text{eq}}^{(O)}}_{\Pi^{(O)}} + \underbrace{\frac{1}{|\Omega|}\int_{\mathcal{S}_d} \left|\Delta \underline{v}\right| \sigma_0 d_{\text{eq}}^{(I)}}_{\Pi^{\text{surf}}} \tag{13}$$

Strain rates related to the trial velocity field are taken from Torki et al. (2023):

$$\begin{array}{lll} d_{\rho\rho}^{(O)} = -\dfrac{1}{2}\left(\dfrac{R^2}{\rho^2}D_{kk} + D_{33}\right) & d_{\theta\theta}^{(O)} = \dfrac{1}{2}\left(\dfrac{R^2}{\rho^2}D_{kk} - D_{33}\right) & d_{zz}^{(O)} = D_{33} \\ d_{\rho\rho}^{(P)} = \dfrac{1}{2}\left(\dfrac{1}{\chi^2}D_{kk} - D_{33}\right) & d_{\theta\theta}^{(P)} = \dfrac{1}{2}\left(\dfrac{1}{\chi^2}D_{kk} - D_{33}\right) & d_{zz}^{(P)} = D_{33} - \dfrac{1}{\chi^2}D_{kk} \end{array} \tag{14}$$

The tangential velocity jump on $\mathcal{S}_d$ is along $\underline{e}_3$:

$$\left|\Delta\underline{v}\right| = \frac{H-z}{\chi^2}\,|D_{kk}| \tag{15}$$

Eq. 13 requires to perform the integration of the equivalent strain rate d_{eq}, which depends on cylindrical coordinate ρ (or z) due to $\boldsymbol{d}$ and on θ due to tensor $\hat{\mathbb{h}}$. At fixed ρ (or z), the θ-integral of d_{eq} do not admit an analytic expression in general; resorting to Cauchy-Schwarz inequality yields:

$$\frac{1}{2\pi}\int_0^{2\pi} d_{\text{eq}}(\rho,\theta)\,\mathrm{d}\theta \leq \sqrt{\frac{1}{2\pi}\int_0^{2\pi} d_{\text{eq}}^2(\rho,\theta)\,\mathrm{d}\theta} \equiv \sqrt{\left\langle d_{\text{eq}}^2\right\rangle_\theta(\rho)} \tag{16}$$

Note that if $\hat{\mathbb{h}}$ does not depend on θ (*i.e.* transverse isotropy), then inequality turns into equality. Writing $\hat{\mathbb{h}}$ in the cylindrical frame of reference, lengthy but elementary evaluation leads to:

$$\left\langle\left(d_{\text{eq}}^{(\text{O})}\right)^2\right\rangle_\theta = \hat{h}_q D_{33}^2 + \frac{\hat{h}_t}{3}\left(\frac{R}{\rho}\right)^4 D_{kk}^2\ ,\quad \left\langle\left(d_{\text{eq}}^{(\text{P})}\right)^2\right\rangle_\theta = \hat{h}_q\left(\frac{1}{\chi^2}D_{kk} - D_{33}\right)^2\ ,\quad \left\langle\left(d_{\text{eq}}^{(\text{I})}\right)^2\right\rangle_\theta = \frac{\hat{h}_a}{3} \tag{17}$$

where $\hat{h}_q$, $\hat{h}_t$ and $\hat{h}_a$ are scalar anisotropy factors also used in the anisotropic yield criteria of Benzerga and Besson (2001) and Keralavarma and Benzerga (2010) (void growth) as well as Keralavarma and Chockalingam (2016) (coalescence in layers). They are related to the coefficients of the Voigt-Mandel representation of $\hat{\mathbb{h}}$ and, as expected, are left unchanged by rotations of the frame of reference around void axis $\underline{e}_3$:

$$\hat{h}_q = \frac{\hat{h}_{11}+\hat{h}_{22}+4\hat{h}_{33}-4\hat{h}_{23}-4\hat{h}_{31}+2\hat{h}_{12}}{6}\ ,\quad \hat{h}_t = \frac{\hat{h}_{11}+\hat{h}_{22}+2\hat{h}_{66}-2\hat{h}_{12}}{4}\ ,\quad \hat{h}_a = \frac{\hat{h}_{44}+\hat{h}_{55}}{2} \tag{18}$$

After straightforward integration, volume terms of the macroscopic dissipation write:

$$\begin{gathered}\Pi^{(\text{P})} = \sigma_0(1-c)\sqrt{\hat{h}_q}\left|D_{kk}-\chi^2 D_{33}\right|\ ,\quad \Pi^{(\text{O})} = \sigma_0\left[\sqrt{\frac{\hat{h}_t}{3}}\mathcal{A}\left(\sqrt{\frac{\hat{h}_t}{3\hat{h}_q}}\xi\right)|D_{kk}| + \sqrt{\hat{h}_q}\mathcal{B}\left(\sqrt{\frac{\hat{h}_t}{3\hat{h}_q}}\xi\right)|D_{33}|\right]\\ \text{where}\quad \xi = \frac{D_{kk}}{D_{33}}\quad\text{and}\quad \begin{cases}\mathcal{A}(x) & = \log\left[\dfrac{x^2}{\chi^2}\left(-1+\sqrt{1+\dfrac{1}{x^2}}\right)\left(1+\sqrt{1+\dfrac{\chi^4}{x^2}}\right)\right]\\ \mathcal{B}(x) & = \sqrt{1+x^2}-\sqrt{\chi^4+x^2}\end{cases}\end{gathered} \tag{19}$$

Finally, using Eqs. 5 and 15, the surface term reads:

$$\Pi^{\text{surf}} = \frac{\sigma_0}{\pi R^2 H}\frac{|D_{kk}|}{\chi^2}\int_h^H 2\pi r(H-z)\sqrt{\left\langle\left(d_{\text{eq}}^{(\text{I})}\right)^2\right\rangle_\theta}\,\mathrm{d}z = \frac{\sigma_0}{\sqrt{3}}\frac{w}{c}(1-c)^2\sqrt{\hat{h}_a}\,|D_{kk}| \tag{20}$$

For an isotropic Von Mises matrix $\hat{h}_q = \hat{h}_t = \hat{h}_a = 1$, so Eqs. 19 and 20 recover the expressions found in Torki et al. (2023).

3.1.2. Yield criterion

Eqs. 6-8 are used to obtain the yield surface; under axisymmetric loading, Eq. 6 can be written:

$$\boldsymbol{\Sigma} : \boldsymbol{D} = \Sigma_{\rho\rho}D_{kk} + (\Sigma_{33}-\Sigma_{\rho\rho})D_{33} \tag{21}$$

Two cases should be considered depending on the differentiability of Π. $\Pi^{(\text{O})}$ is a differentiable function of (D_{kk}, D_{33}) on $\mathbb{R}^2 \setminus \{(0,0)\}$ whereas Π^{surf} is non-differentiable on strain rates verifying $D_{kk} = 0$ and $\Pi^{(\text{P})}$ is non-differentiable on strain rates verifying $D_\chi \equiv D_{kk} - \chi^2 D_{33} = 0$. Thus, the condition of differentiability on Π is $D_{kk}D_\chi \neq 0$. For cases where Π is differentiable, Eq. 7 specifies into[1]:

$$\begin{aligned}\Sigma_{\rho\rho} = \frac{\partial\Pi}{\partial D_{kk}} &= \text{sgn}(D_{33})\,\sigma_0\left[\text{sgn}(\xi-\chi^2)(1-c)\sqrt{\hat{h}_q} + \text{sgn}(\xi)\left(\sqrt{\frac{\hat{h}_t}{3}}\mathcal{A}\left(\sqrt{\frac{\hat{h}_t}{3\hat{h}_q}}\xi\right) + \frac{w}{\sqrt{3}}\frac{(1-c)^2}{c}\sqrt{\hat{h}_a}\right)\right]\\ \Sigma_{33}-\Sigma_{\rho\rho} = \frac{\partial\Pi}{\partial D_{33}} &= \text{sgn}(D_{33})\,\sigma_0\left[-\text{sgn}(\xi-\chi^2)(1-c)\chi^2\sqrt{\hat{h}_q} + \sqrt{\hat{h}_q}\mathcal{B}\left(\sqrt{\frac{\hat{h}_t}{3\hat{h}_q}}\xi\right)\right]\end{aligned} \tag{22}$$

which gives a parametrization of the yield surface in terms of $\xi \in \mathbb{R}$ and $\text{sgn}(D_{33})$. Next, simple algebra can eliminate parameter ξ in Eq. 22 in order to obtain a closed-form of the yield criterion. First, the fact that $\cosh(\log x) = \left(x + x^{-1}\right)/2$ leads to:

$$\cosh\mathcal{A} = \frac{1}{\chi^2}\left[\sqrt{1+\xi^2}\sqrt{\chi^4+\xi^2}-\xi^2\right] \tag{23}$$

---

[1] Remark that terms related to $\mathcal{A}'$ and $\mathcal{B}'$ cancel out because $\mathcal{A}'(x) = -|x|\,\mathcal{B}'(x)$.

which, using $\mathcal{B}$, can be rewritten as a Gurson-like criterion, χ^2 being the relative volume occupied by the central zone:

$$\mathcal{B}^2 + 2\chi^2 \cosh \mathcal{A} - (1 + \chi^4) = 0 \tag{24}$$

Inversion of the linear system of Eq. 22 in order to express $(\mathcal{A}, \mathcal{B})$ according to $(\Sigma_{\rho\rho}, \Sigma_{33} - \Sigma_{\rho\rho})$ lead to the following family of criteria:

$$\left[\sqrt{\frac{1}{\hat{h}_q}} \frac{\Sigma_{33} - \Sigma_{\rho\rho}}{\sigma_0} + \epsilon_1 (1-c)\chi^2\right]^2 + 2\chi^2 \cosh\left[\sqrt{\frac{3}{\hat{h}_t}} \left(\frac{\Sigma_{\rho\rho}}{\sigma_0} - \epsilon_1 (1-c)\sqrt{\hat{h}_q} - \epsilon_2 \frac{w}{\sqrt{3}} \frac{(1-c)^2}{c} \sqrt{\hat{h}_a}\right)\right] - (1 + \chi^4) = 0 \tag{25}$$

where $\epsilon_1 = \text{sgn}(D_\chi)$ and $\epsilon_2 = \text{sgn}(D_{kk})$. Thus, Eq. 25 corresponds to four parts on the yield surface.

Then, the zones where Π is not differentiable are considered. The case in which $D_{kk} = 0$ and $D_\chi \neq 0$ is considered, which corresponds to $\xi = 0$. Since $\Pi(D_{kk}, D_{33})$ is differentiable in the second variable and left- and right- differentiable in the first variable, the subdifferential writes:

$$\partial\Pi(0, D_{33}) = \left[\left.\frac{\partial\Pi}{\partial D_{kk}}\right|_{0^-} (0, D_{33}),\ \left.\frac{\partial\Pi}{\partial D_{kk}}\right|_{0^+} (0, D_{33})\right] \times \left\{\frac{\partial\Pi}{\partial D_{33}}(0, D_{33})\right\} \tag{26}$$

so that Eq. 8 yields:

$$\left|\Sigma_{\rho\rho} + \text{sgn}(D_{33})\sigma_0(1-c)\sqrt{\hat{h}_q}\right| \leq \sigma_0 \frac{w}{\sqrt{3}} \frac{(1-c)^2}{c} \sqrt{\hat{h}_a}\ ,\quad \Sigma_{33} - \Sigma_{\rho\rho} = \text{sgn}(D_{33})\sigma_0 \sqrt{\hat{h}_q}\left(1 - c\chi^2\right) \tag{27}$$

The case in which $D_\chi = 0$ ($\xi = \chi^2$) and $D_{kk} \neq 0$ (or alternatively $D_{33} \neq 0$) can be treated by recasting Π as a function of D_χ and D_{33}. Since $\boldsymbol{\Sigma} : \boldsymbol{D} = \Sigma_{\rho\rho} D_\chi + \left(\Sigma_{33} - (1-\chi^2)\Sigma_{\rho\rho}\right) D_{33}$, Eq. 8 writes:

$$\left(\Sigma_{\rho\rho}, \Sigma_{33} - (1-\chi^2)\Sigma_{\rho\rho}\right) \in \partial\Pi(0, D_{33}) = \left[\left.\frac{\partial\Pi}{\partial D_\chi}\right|_{0^-} (0, D_{33}),\ \left.\frac{\partial\Pi}{\partial D_\chi}\right|_{0^+} (0, D_{33})\right] \times \left\{\frac{\partial\Pi}{\partial D_{33}}(0, D_{33})\right\} \tag{28}$$

which means that

$$\begin{gathered}\left|\Sigma_{\rho\rho} - \text{sgn}(D_{33})\sigma_0\left[\sqrt{\frac{\hat{h}_t}{3}}\mathcal{A}\left(\sqrt{\frac{\hat{h}_t}{3\hat{h}_q}}\chi^2\right) + \frac{w}{\sqrt{3}}\frac{(1-c)^2}{c}\sqrt{\hat{h}_a}\right]\right| \leq \sigma_0(1-c)\sqrt{\hat{h}_q} \\ \Sigma_{33} - (1-\chi^2)\Sigma_{\rho\rho} = \text{sgn}(D_{33})\sigma_0\left[\sqrt{\frac{\hat{h}_t}{3}}\chi^2\mathcal{A}\left(\sqrt{\frac{\hat{h}_t}{3\hat{h}_q}}\chi^2\right) + \sqrt{\hat{h}_q}\mathcal{B}\left(\sqrt{\frac{\hat{h}_t}{3\hat{h}_q}}\chi^2\right) + \frac{1}{\sqrt{3}}\frac{w}{c}(1-c)^2\chi^2\sqrt{\hat{h}_a}\right]\end{gathered} \tag{29}$$

Eqs. 27 and 29 together describe four plat parts which complete the yield surface by connecting the four curved parts described previously.

The yield surface is therefore described by the conjunction of Eqs. 22, 27 and 29; this is one of the main results of this study. It can be verified that the surface is continuous; indeed, Eq. 22 is compatible with Eq. 27 when D_{kk} goes to 0, and compatible with Eq. 29 when D_χ goes to 0. In fact, it is fully differentiable, as shown in Morin et al. (2016a). A graphical representation of the obtained yield criterion in the meridian plane $\left(\Sigma_\text{m}, \Sigma_{33} - \Sigma_{\rho\rho}\right)$ where $\Sigma_\text{m} \equiv \Sigma_{kk}/3$ is provided in Fig. 5. The yield surface displays four different modes of deformation:

- a homogeneous yielding mode (Eq. 27) where $\text{tr}(\boldsymbol{D}) = 0$, meaning that the volume of void will not change;
- a heterogeneous yielding mode (Eq. 22 with $0 < \xi < \chi^2$), in which plasticity happens preferentially in the outer zone;
- a heterogeneous yielding mode (Eq. 22 with $\xi < 0$ or $\xi > \chi^2$), in which plasticity happens preferentially in the plugs;
- a localized yielding mode (Eq. 29) in which plasticity occurs exclusively in the outer zone, *i.e.* a hollow cylinder, while the plugs are elastically unloaded;

In the literature, the first two deformation modes are generally described as void growth (in this study, the first one will be distinguished and denoted *void stabilization* for convenience) and the third one is denoted as coalescence in columns (*e.g.* Torki et al. (2023)). The fourth deformation mode has been discussed less frequently but previous evidence have been collected through unit-cell simulations (Chouksey et al., 2019, 2020; Chouksey and Basu, 2021); since no clear denomination has emerged, it shall be denoted *columnar shielding* in the remainder of the study.

Some limit behaviors are worth considering in order to compare the criterion to known theoretical results. When χ goes to 0 — *i.e.* no porosity — Eq. 25, 27_b and 29_b all lead to the same expression $\left|\Sigma_{33} - \Sigma_{\rho\rho}\right| = \sqrt{\hat{h}_q}\sigma_0$, which is Hill's criterion. When c goes to 0, Eq. 27 yields the same result. When c goes to 1, Eq. 25 recovers the anisotropic criterion of Benzerga and Besson (2001) for a hollow cylinder (whereas Eq. 27 and 29 reduce to sub-cases of Eq. 25). Finally when χ goes to 1, the curved parts of Eq. 23 reduce to points; thus, only the flat parts remains. On the one-hand, Eq. 27_b becomes

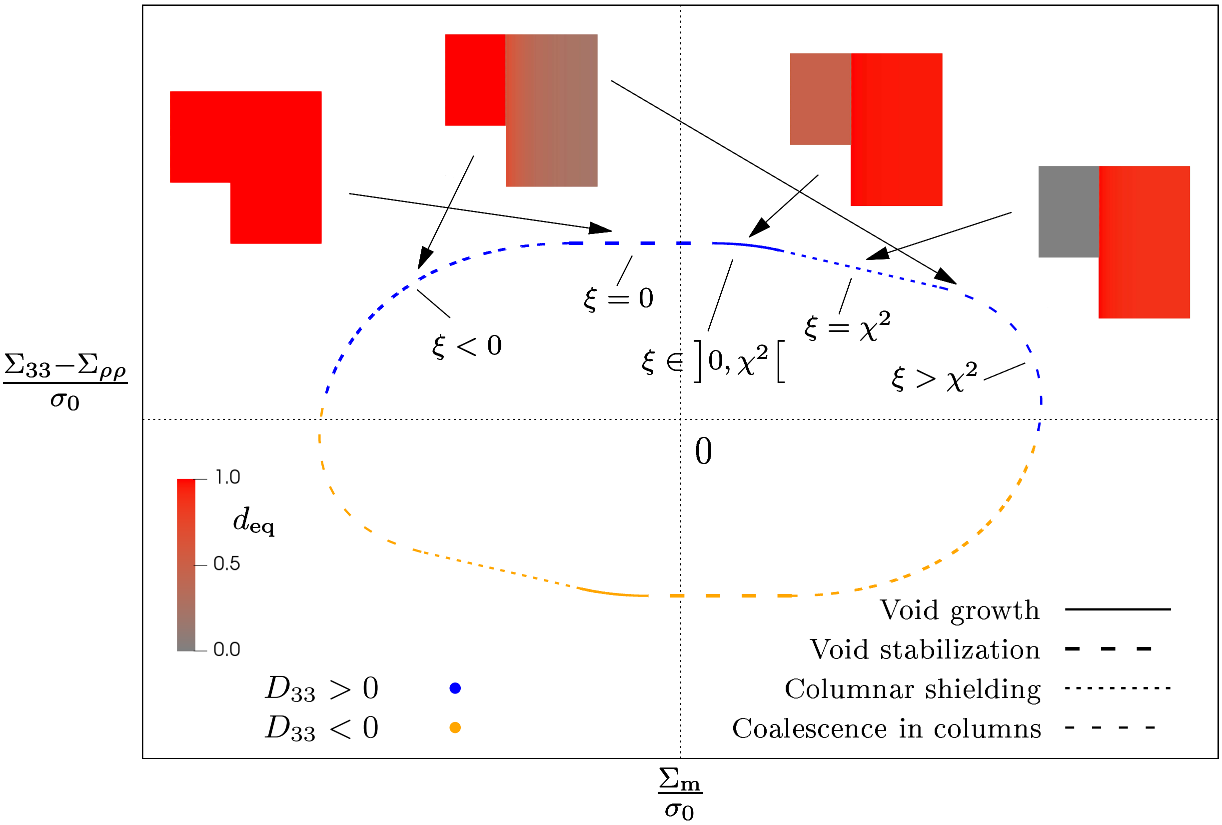

Figure 5: Sketch of the yield surface associated with the trial field defined by Eq. 12. Each section of the yield surface is linked to the deformation mode experienced by the unit-cells; the corresponding equivalent deformation maps are shown (with d_{eq} normalized so its maximum is 1) for an isotropic material. The values of the strain ratio ξ and the sign of D_{33} are also displayed on the graph.

$\left|\Sigma_{33} - \Sigma_{\rho\rho}\right| = (1-c)\sqrt{\hat{h}_q}\sigma_0$ which is comfortingly Hill's criterion for the remaining upper (or lower) cylinder. On the other hand, a positive yield limit on $|\Sigma_{33}|$ is predicted by Eq. 29_b, which is unphysical because the voided horizontal band should imply $\Sigma_{33} = 0$. This is explained by the fact that the discontinuity surface $\mathcal{S}_d$ no longer exists when $\chi = 1$ so that Π^{surf} should vanish, allowing to recover $\Sigma_{33} = 0$

It can then be useful to specialize the criterion for cracks through extreme values of w: needle-like (*i.e.* one-dimensional) when w goes to infinity, in which case the criterion becomes $\left|\Sigma_{33} - \Sigma_{\rho\rho}\right| = \sqrt{\hat{h}_q}\sigma_0(1-c\chi^2)$, and penny-shaped (*i.e* two-dimensional) when w goes to 0, in which case one of the two flat parts (Eq. 27) of the criterion disappears.

It is shown in Fig. 6a that χ, c and w all have a significant influence on the yield criterion. Although the figure is plotted for an isotropic material, the trends it displays also hold for anisotropic materials. Increasing χ induces a contraction of the yield surface as well as a noticeable shape change of the columnar shielding section since χ controls directly the slope of the slanted straight-lined part (Eq. 29_b). As expected, increasing c has also a strong damaging effect and this change dominates the one induced by χ as far as coalescence in columns is concerned. Finally, increasing w expands the yield surface at high stress triaxiality ratios, meaning that coalescence in columns and columnar shielding are hindered for prolate voids compared to oblate voids, but that void growth and stabilization are left unaffected by the aspect ratio of the cavity. This is coherent with the fact that void growth is known to be affected only by void volume fraction $f = c\chi^2$ upon which w has no influence.

The influence of the three coefficients $\hat{h}_q$, $\hat{h}_t$, $\hat{h}_a$ that characterize the anisotropy of the matrix relatively to velocity fields is shown in Fig. 6b. Increasing one of these values results in the extension of the yield surface, but modes of expansion are different. In the case of $\hat{h}_a$ and $\hat{h}_t$, this effect is restricted to rather high stress triaxiality ratios, *i.e.* the section where coalescence in columns is active. It is noticed that $\hat{h}_t$ has a stronger influence than $\hat{h}_a$, except on columnar shielding (Eq. 29_b). In the case of $\hat{h}_q$, the effect on the yield surface is somehow uniform, which means that it affects both void stabilization, columnar shielding and coalescence in columns; note that the slanted part accounting for columnar shielding (Eq. 29_a) occupies a larger section of the yield surface.

3.2. From homogeneous yielding to inhomogeneous yielding in layers

In this section, the transition from homogeneous yielding (Fig. 1a) to internal necking (Fig. 1b) is accounted for using a dedicated yield surface describing the gradual localization of strain in layers perpendicular to the main loading axis. This yield surface is therefore an extension of the work of Morin et al. (2016a) to anisotropic materials following Hill's criterion (Eq. 10).

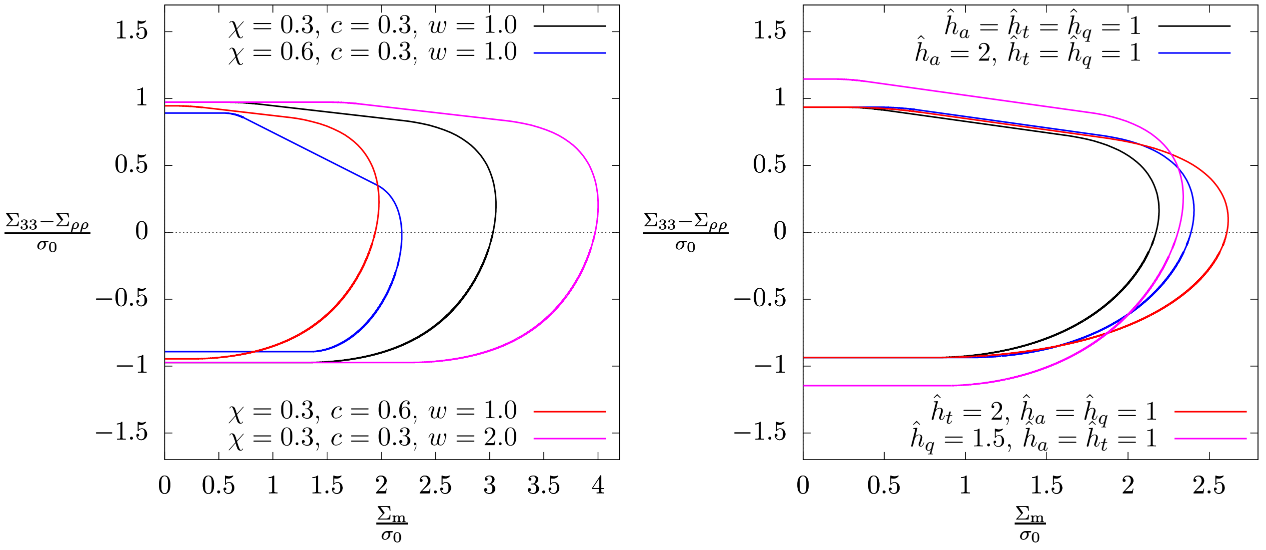

(a) (b)

Figure 6: Graphical investigation of the yield criterion: (a) effect of the geometry on the yield surface in the isotropic case ($\hat{h}_q = \hat{h}_t = \hat{h}_a = 1$); (b) effect of the anisotropy factors on the yield surface at $\chi = c = 0.4$ and $w = 1$.

3.2.1. *Trial velocity field and associated plastic dissipation*

The trial velocity field proposed in Morin et al. (2016a) accounts for the situations depicted in Fig. 1a,b and is defined in the geometry shown in Fig. 4b:

$$\begin{array}{lll} \text{Ligament:} & v_\rho^{(L)}(\rho) = \dfrac{1}{2}\left\{\dfrac{D_{kk}}{c}\dfrac{R^2}{\rho} - \left[\left(\dfrac{1}{c}-1\right)D_{kk} + D_{33}\right]\rho\right\} \ , & v_z^{(L)}(z) = \left[\left(\dfrac{1}{c}-1\right)D_{kk} + D_{33}\right]z \\ \text{Outer zone:} & v_\rho^{(E)}(\rho) = \dfrac{1}{2}\left(D_{kk} - D_{33}\right)\rho \ , & v_z^{(E)}(z) = (D_{33} - D_{kk})z + HD_{kk} \end{array} \tag{30}$$

This trial velocity field is incompressible, kinematically admissible with Eq. 2, and displays a purely tangential discontinuity at the interface $\mathcal{S}_d$ $(z = h)$. As this field has been shown in Morin et al. (2016a) to lead to results in good agreement with numerical simulations for isotropic materials, it will be adopted to study general anisotropic materials. In the transverse ligament (L) and the outer zone (E), the strain rates associated with this trial field write:

$$\begin{array}{lll} d_{\rho\rho}^{(L)} = -\dfrac{1}{2}\left[\dfrac{D_{kk}}{c}\left(\dfrac{R^2}{\rho^2} + (1-c)\right) + D_{33}\right] & d_{\theta\theta}^{(L)} = \dfrac{1}{2}\left[\dfrac{D_{kk}}{c}\left(\dfrac{R^2}{\rho^2} - (1-c)\right) - D_{33}\right] & d_{zz}^{(L)} = \dfrac{1-c}{c}D_{kk} + D_{33} \\ d_{\rho\rho}^{(E)} = \dfrac{1}{2}\left(D_{kk} - D_{33}\right) & d_{\theta\theta}^{(E)} = \dfrac{1}{2}\left(D_{kk} - D_{33}\right) & d_{zz}^{(E)} = D_{33} - D_{kk} \end{array} \tag{31}$$

The tangential velocity jump at $\mathcal{S}_d$ writes (see Appendix C of Morin et al. (2016a)):

$$\left|\Delta \underline{v}\right| = \frac{D_{kk}}{2c}\left(\frac{R^2}{\rho} - \rho\right) \tag{32}$$

Next, computations are similar to those that brought Eq. 17:

$$\left\langle\left(d_{\text{eq}}^{(L)}\right)^2\right\rangle_\theta = \hat{h}_q\left(\frac{1-c}{c}D_{kk} + D_{33}\right)^2 + \frac{\hat{h}_t}{3}\left(\frac{R}{\rho}\right)^4\left(\frac{D_{kk}}{c}\right)^2 \ , \ \left\langle\left(d_{\text{eq}}^{(E)}\right)^2\right\rangle_\theta = \hat{h}_q\left(D_{kk} - D_{33}\right)^2 \ , \ \left\langle\left(d_{\text{eq}}^{(I)}\right)^2\right\rangle_\theta = \frac{\hat{h}_a}{3} \tag{33}$$

which combine into the following upper bound for the macroscopic dissipation:

$$\Pi = \Pi^{(E)} + \Pi^{(L)} + \Pi^{\text{surf}} \tag{34}$$

where dissipation terms write:

$$\begin{array}{c} \Pi^{(E)} = \sigma_0(1-c)\sqrt{\hat{h}_q}\left|D_{kk} - D_{33}\right| \quad , \quad \Pi^{\text{surf}} = \sigma_0\dfrac{\chi^3 - 3\chi + 2}{3\sqrt{3}w\chi}\sqrt{\hat{h}_a}\left|D_{kk}\right| \\ \Pi^{(L)} = \sigma_0\left[\sqrt{\dfrac{\hat{h}_t}{3}}\mathcal{A}\left(\sqrt{\dfrac{\hat{h}_t}{3\hat{h}_q}}\dfrac{\xi}{\bar{\xi}}\right)\left|D_{kk}\right| + \sqrt{\hat{h}_q}\mathcal{B}\left(\sqrt{\dfrac{\hat{h}_t}{3\hat{h}_q}}\dfrac{\xi}{\bar{\xi}}\right)\left|(1-c)D_{kk} + cD_{33}\right|\right] \quad \text{with} \quad \bar{\xi} = (1-c)\xi + c \end{array} \tag{35}$$

3.2.2. *Yield criterion*

The yield surface is obtained from the fundamental equation of limit-analysis (Eq. 6) following the path laid in Section 3.1.2. $\Pi^{(E)}$ is non-differentiable when $D_{kk} - D_{33} = 0$, Π^{surf} when $D_{kk} = 0$ and $\Pi^{(L)}$ when $D_{kk} = D_{33} = 0$. For cases where Π is differentiable, *i.e.* $D_{kk}(D_{kk} - D_{33}) \neq 0$, the yield criterion is written in parametric form as[2]:

$$\begin{aligned} \Sigma_{33} - \Sigma_{\rho\rho} &= \frac{\partial \Pi}{\partial D_{33}} = \mathrm{sgn}(D_{33})\,\sigma_0 \left[-\mathrm{sgn}(\xi - 1)(1-c)\sqrt{\hat{h}_q} + \mathrm{sgn}(\bar{\xi}) c \sqrt{\hat{h}_q}\mathcal{B}\left(\sqrt{\frac{\hat{h}_t}{3\hat{h}_q}\frac{\xi}{\bar{\xi}}} \right) \right] \\ \Sigma_{33} &= \frac{\partial \Pi}{\partial D_{33}} + \frac{\partial \Pi}{\partial D_{kk}} = \mathrm{sgn}(D_{33})\,\sigma_0 \left\{ \mathrm{sgn}(\bar{\xi}) \sqrt{\hat{h}_q}\mathcal{B}\left(\sqrt{\frac{\hat{h}_t}{3\hat{h}_q}\frac{\xi}{\bar{\xi}}} \right) + \mathrm{sgn}(\xi) \left[\sqrt{\frac{\hat{h}_t}{3}}\mathcal{A}\left(\sqrt{\frac{\hat{h}_t}{3\hat{h}_q}\frac{\xi}{\bar{\xi}}} \right) + \frac{\chi^3 - 3\chi + 2}{3\sqrt{3}w\chi}\sqrt{\hat{h}_a} \right] \right\} \end{aligned} \tag{36}$$

which can be rewritten using Eq. 23 as:

$$\left[\sqrt{\frac{1}{\hat{h}_q}} \frac{\Sigma_{33} - \Sigma_{\rho\rho}}{c\sigma_0} + \epsilon_3 \frac{1-c}{c} \right]^2 + 2\chi^2 \cosh\left[\sqrt{\frac{3}{\hat{h}_t}} \left(\frac{\Sigma_{\rho\rho} - (1-c)\Sigma_{33}}{c\sigma_0} - \epsilon_3 \frac{1-c}{c}\sqrt{\hat{h}_q} - \epsilon_2 \frac{\chi^3 - 3\chi + 2}{3\sqrt{3}cw\chi}\sqrt{\hat{h}_a} \right) \right] - (1 + \chi^4) = 0 \tag{37}$$

where $\epsilon_3 = \mathrm{sgn}(D_{\rho\rho})$.

For cases where Π is not differentiable, the same method used in Section 3.1.2 is followed to get the corresponding parts of the yield criterion. When $D_{kk} = 0$ ($\xi = 0$) and $D_{kk} - D_{33} \neq 0$, it is obtained that:

$$\left| \Sigma_{\rho\rho} + \mathrm{sgn}(D_{33})\sigma_0(1-c)\chi^2\sqrt{\hat{h}_q} \right| \leq \sigma_0 \frac{\chi^3 - 3\chi + 2}{3\sqrt{3}w\chi}\sqrt{\hat{h}_a} \quad , \quad \Sigma_{33} - \Sigma_{\rho\rho} = \mathrm{sgn}(D_{33})\sigma_0\sqrt{\hat{h}_q}\left(1 - c\chi^2\right) \tag{38}$$

whereas $D_{kk} - D_{33} = 0$ ($\xi = 1$) and $D_{kk} \neq 0$ leads to:

$$\begin{aligned} &\left| \Sigma_{33} - \Sigma_{\rho\rho} - \mathrm{sgn}(D_{33})c\sigma_0\mathcal{B}\left(\sqrt{\frac{\hat{h}_t}{3\hat{h}_q}} \right)\sqrt{\hat{h}_q} \right| \leq \sigma_0(1-c)\sqrt{\hat{h}_q} \\ &\Sigma_{33} = \mathrm{sgn}(D_{33})\sigma_0 \left[\sqrt{\frac{\hat{h}_t}{3}}\mathcal{A}\left(\sqrt{\frac{\hat{h}_t}{3\hat{h}_q}} \right) + \sqrt{\hat{h}_q}\mathcal{B}\left(\sqrt{\frac{\hat{h}_t}{3\hat{h}_q}} \right) + \frac{\chi^3 - 3\chi + 2}{3\sqrt{3}w\chi}\sqrt{\hat{h}_a} \right] \end{aligned} \tag{39}$$

A graphical representation of the obtained yield criterion in the meridian plane $\left(\Sigma_{\mathrm{m}}, \Sigma_{33} - \Sigma_{\rho\rho}\right)$ is provided in Fig. 7. The yield surface displays three different modes of deformation:

- a homogeneous yielding mode (Eq. 38) where $\mathrm{tr}(\boldsymbol{D}) = 0$, meaning that the volume of void will not change;
- a heterogeneous yielding mode (Eq. 36), in which plasticity happens preferentially in the transverse ligament, inducing a change of porosity (positive to the right-hand side of the homogeneous part and negative to the left-hand side);
- a localized yielding mode (Eq. 39), in which plasticity occurs exclusively in the transverse ligament while the upper and the lower zones are elastically unloaded.

In the literature, the first two deformation modes are generally described as void growth (in this study, the first one will be distinguished and denoted *void stabilization* for convenience) whereas the last one corresponds to internal necking (*e.g.* Morin et al. (2016a)).

Again, some limit behaviors are worth considering in order to compare the criterion to known theoretical results. When χ goes to 0 — *i.e.* no porosity — the yield criterion reduces to Hill's criterion $\left|\Sigma_{33} - \Sigma_{\rho\rho}\right| = \sqrt{\hat{h}_q}\sigma_0$. When χ goes to 1, Eq. 37 yield $\Sigma_{33} = 0$ and $\left|\Sigma_{\rho\rho}\right| = \sigma_0\sqrt{\hat{h}_q}(1-c)$ which is exactly what may be expected from a Hill material laminated with void along $\underline{e}_z$. When c goes to 1, Eq. 37 recovers the anisotropic criterion of Benzerga and Besson (2001) for a hollow cylinder whereas Eqs. 38-39 reduce to points. When c goes to 0, Eq. 37 reduces to points so the yield surface becomes a parallelogram whose sides are Hill's criterion (from Eq. 38) since the material has no porosity and an anisotropic version of the internal necking criterion of Benzerga and Leblond (2014) (from Eq. 39) because the material can still coalesce in a horizontal plane without prior void growth.

The criterion can be used to make novel predictions for cracks by considering extreme values of w. Needle-like (*i.e.* one-dimensional) cracks are obtained when w goes to infinity, in which case the criterion becomes one of the two flat parts (Eq. 38) of the criterion disappears. Penny-shaped (*i.e* two-dimensional) cracks when w goes to 0, in which case the criterion becomes $\left|\Sigma_{33} - \Sigma_{\rho\rho}\right| = \sqrt{\hat{h}_q}\sigma_0(1 - c\chi^2)$. This is an oversimplification since internal necking still occurs for penny-shaped cracks, as shown in Hure and Barrioz (2016); this discrepancy emerges from the fact that when $w = 0$, the trial field cannot accommodate the axial strain rate D_{33} due to the absence of transverse ligament.

For isotropic materials, the internal necking criterion (Eq. 39) becomes:

$$\Sigma_{33} = \mathrm{sgn}(D_{33})\sigma_0 \left[\frac{1}{\sqrt{3}}\mathcal{A}\left(\frac{1}{\sqrt{3}}\right) + \mathcal{B}\left(\frac{1}{\sqrt{3}}\right) + \frac{\chi^3 - 3\chi + 2}{3\sqrt{3}w\chi} \right] \tag{40}$$

---

[2] See footnote 1.

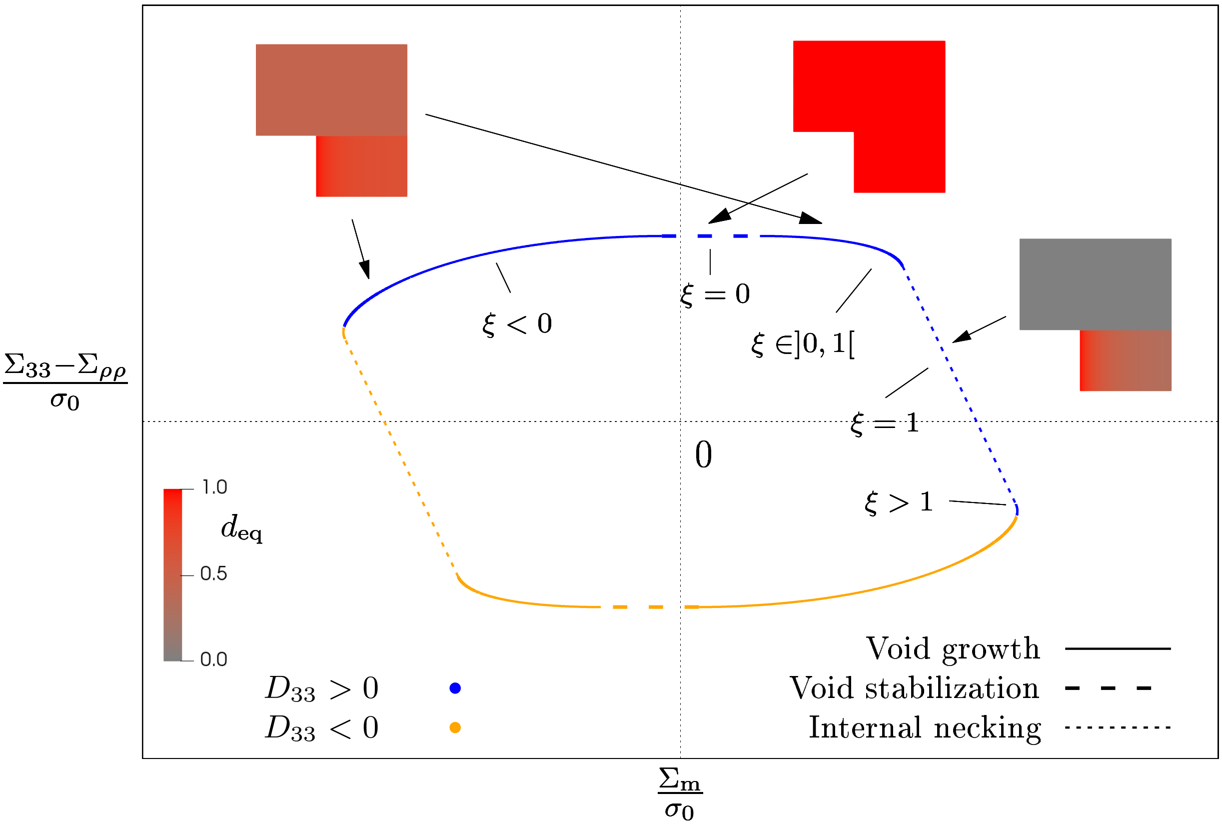

Figure 7: Sketch of the yield surface associated with the trial field defined by Eq. 30. Each section of the yield surface is linked to the deformation mode experienced by the unit-cell; the corresponding equivalent deformation maps are shown (with d_{eq} normalized so its maximum is 1) for an isotropic material. The values of the strain ratio ξ and the sign of D_{33} are also displayed on the graph.

which has been shown by Torki et al. (2015) to require a correction to improve the agreement to numerical results and recover an acceptable yield criterion in the limit $w \to 0$. The calibration led in the aforementioned study resulted in the multiplication of the third term of Eq. 40 by a function t given by:

$$t(x,\chi) = \frac{(t_0 + t_1\chi)w}{1 + (t_0 + t_1\chi)w} \quad \text{where} \quad (t_0, t_1) = (-0.84, 12.9) \tag{41}$$

Note that the parameter b introduced in Torki et al. (2015) is discarded since it would induce uncontrolled shape changes in the yield surface. The correction for isotropic materials (Eq. 41) is extended to anisotropic materials in by replacing $\sqrt{\hat{h}_a}$ by $t(w,\chi)\sqrt{\hat{h}_a}$ in Eqs. 37, 38 and 39.

The yield surface is strongly dependent on microstructure parameters, as seen in Fig. 8a. On the one-hand, the internal necking section (Eq. 39) is determined fully by w and χ, as shown in the original study of Benzerga and Leblond (2014). Increasing any of those parameters results in the shrinking of the yield surface, mainly through the shift of the straight-lined part. Note that the effect of w on columnar localization is the opposite of the one it has on layered localization since internal necking is promoted by prolate voids. On the other hand, the void stabilization part does not depend on w and is mainly determined by the value of c. The effect of anisotropy factors on the yield surface is shown in Fig. 8b; these parameters appear to have the same qualitative influence on the yield surface as they did in Fig. 6b: $\hat{h}_q$ has a rather homogeneous effect no matter the triaxiality whereas $\hat{h}_a$ and $\hat{h}_t$ only modify the high-triaxiality section (*i.e* coalescence).

As stated at the beginning of Section 3, the complete yield criterion for porous Hill materials under axisymmetric loading is obtained by combining the two yield criteria obtained in Section 3.1.2 and Section 3.2.2 using the multi-surface framework described in Benzerga and Leblond (2010). In this framework, the final elasticity domain is the intersection of individual domains associated with the (two) sub-criteria, as shown on Fig 9.

3.3. Numerical assessment

Assessment of the analytical criterion is then performed by resorting to numerical limit-analysis. Small strain finite element simulations are conducted on the unit-cell shown in Fig. 3 using the FEM solver `Cast3M` (CEA, 2022). The displacement is increased linearly while enforcing a fixed stress ratio $\Sigma_{\rho\rho}/\Sigma_{33}$ until small strain yielding of the unit-cell occurs. This manifests by the saturation of $\mathbf{\Sigma}$ to values corresponding to the yield stress of the unit-cell (Madou and Leblond, 2012b).

As in Keralavarma and Chockalingam (2016), the criterion shall be tested on materials whose orthotropy axes are

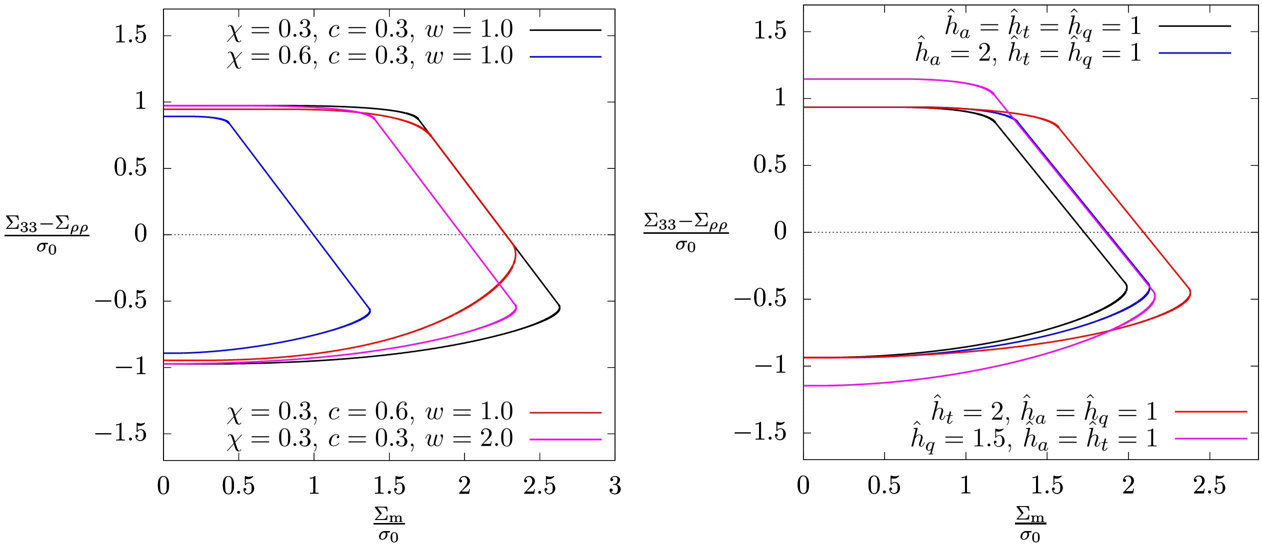

(a)

(b)

Figure 8: Graphical investigation of the yield criterion: (a) effect of the geometry on the yield surface in the isotropic case ($\hat{h}_q = \hat{h}_t = \hat{h}_a = 1$); (b) effect of the anisotropy factors on the yield surface at $\chi = c = 0.4$ and $w = 1$.

aligned with the void axes. In that frame of reference, Hill equivalent stress writes:

$$\begin{aligned}\left(\sigma^{\mathrm{H}}_{\mathrm{eq}}\right)^2 &= \frac{3}{2}\left(h_{11}{\sigma'_{11}}^2 + h_{22}{\sigma'_{22}}^2 + h_{33}{\sigma'_{33}}^2 + 2h_{44}\sigma_{23}^2 + 2h_{55}\sigma_{31}^2 + 2h_{66}\sigma_{12}^2\right)\\ &= \frac{2(h_{11}+h_{22})-h_{33}}{6}(\sigma_{11}-\sigma_{22})^2 + \frac{2(h_{22}+h_{33})-h_{11}}{6}(\sigma_{22}-\sigma_{33})^2 + \frac{2(h_{11}+h_{33})-h_{22}}{6}(\sigma_{11}-\sigma_{33})^2\\ &\qquad + 3h_{44}\sigma_{23}^2 + 3h_{55}\sigma_{31}^2 + 3h_{66}\sigma_{12}^2\end{aligned} \tag{42}$$

where (h_{ij}) are the coefficient of the Voigt-Mandel representation of $\mathbb{h}$.

In the case of transverse isotropy with respect to $\underset{\sim}{e}_3$, equality of yield stress for stress states $\boldsymbol{\sigma} = (\cos\theta)^2 \underset{\sim}{e}_1 \otimes \underset{\sim}{e}_1 + (\sin\theta)^2 \underset{\sim}{e}_2 \otimes \underset{\sim}{e}_2 - 2\cos\theta\sin\theta\, \underset{\sim}{e}_1 \odot \underset{\sim}{e}_2$ brings $h_{11} = h_{22} = h_{66}$. Same considerations about $\boldsymbol{\sigma} = \underset{\sim}{e}_i \odot \underset{\sim}{e}_3$ with $i \in \{1, 2\}$ yield $h_{44} = h_{55}$. These relations also hold for $\hat{\mathbb{h}}$. Taking σ_0 as the transverse yield stress gives $h_{33} = 6 - 5h_{11}$. Thus, material anisotropy can be described by only two parameters that are chosen according to Keralavarma and Chockalingam (2016): the ratio R_a of the axial yield stress relatively to the transverse yield stress and the ratio R_s of the out-of-plane shear yield stress to the transverse yield stress, multiplied by $\sqrt{3}$ to normalize it to 1 in the isotropic case. Using Eq. 42, it can be shown that:

$$R_\mathrm{a} = \frac{1}{\sqrt{4 - 3h_{11}}}\ ,\quad R_\mathrm{s} = \frac{1}{\sqrt{h_{44}}} \tag{43}$$

Then, relationships between coefficients of $\hat{\mathbb{h}}$ and $\mathbb{h}$ bring:

$$\hat{h}_q = R_\mathrm{a}^2\ ,\quad \hat{h}_t = \frac{3R_\mathrm{a}^2}{4R_\mathrm{a}^2 - 1}\ ,\quad \hat{h}_a = R_\mathrm{s}^2 \tag{44}$$

Exploiting the symmetries of the loading as well as those of the material, only a quarter of a section of the unit-cell is effectively simulated under the assumption of axisymmetry. The corresponding mesh is shown on Fig 10a (Fig. 10b will be discussed later); it holds 19200 quadratic quadrangular elements. The material behavior is chosen to elasto-plastic: elasticity is chosen to obey an isotropic Hooke law of Young modulus $Y = 10^3$ MPa and Poisson ratio $\nu = 0.49$ whereas perfect plasticity follows Hill's criterion. As a classical result of limit-analysis, results presented in the following do not depend on elastic parameters. Mesh convergence is duly checked. The displacements of the nodes lying on the boundaries $\mathcal{S}_\mathrm{top}$ and $\mathcal{S}_\mathrm{lat}$ are constrained to have the same vertical (for $\mathcal{S}_\mathrm{top}$) and horizontal (for $\mathcal{S}_\mathrm{lat}$) values consistently with imposing D_{33} and $D_{\rho\rho}$. The macroscopic stress $\boldsymbol{\Sigma}$ is computed by averaging the microscopic stress field $\boldsymbol{\sigma}$ over Ω. Simulations are performed by imposing the displacement on one boundary ($\mathcal{S}_\mathrm{top}$ or $\mathcal{S}_\mathrm{lat}$) and enforcing the ratio of stresses $\Sigma_{\rho\rho}/\Sigma_{33}$ by adjusting the displacement of the other boundary during the iterations of the Newton-Raphson algorithm.

The comparison between numerical yield stresses and the analytical criterion is displayed in Fig. 11. Two unit-cell geometries are studied: on the one hand, $\chi = 0.4$ and $c = 0.4$ (left row of Fig. 11), and on the other hand, $\chi = 0.3$ and $c = 0.6$ (right row of Fig. 11). Both configurations were chosen with a cavity of aspect ratio $w = 1$. In all cases, the numerical results are seen to be interior to the surfaces delimited by the two expressions constituting the yield criterion, confirming their character of upper bound[3].

---

[3] Note that this property is not to be taken for granted in the case of the layered localization surface: indeed, a numerical correction (Eq. 41) was adopted.

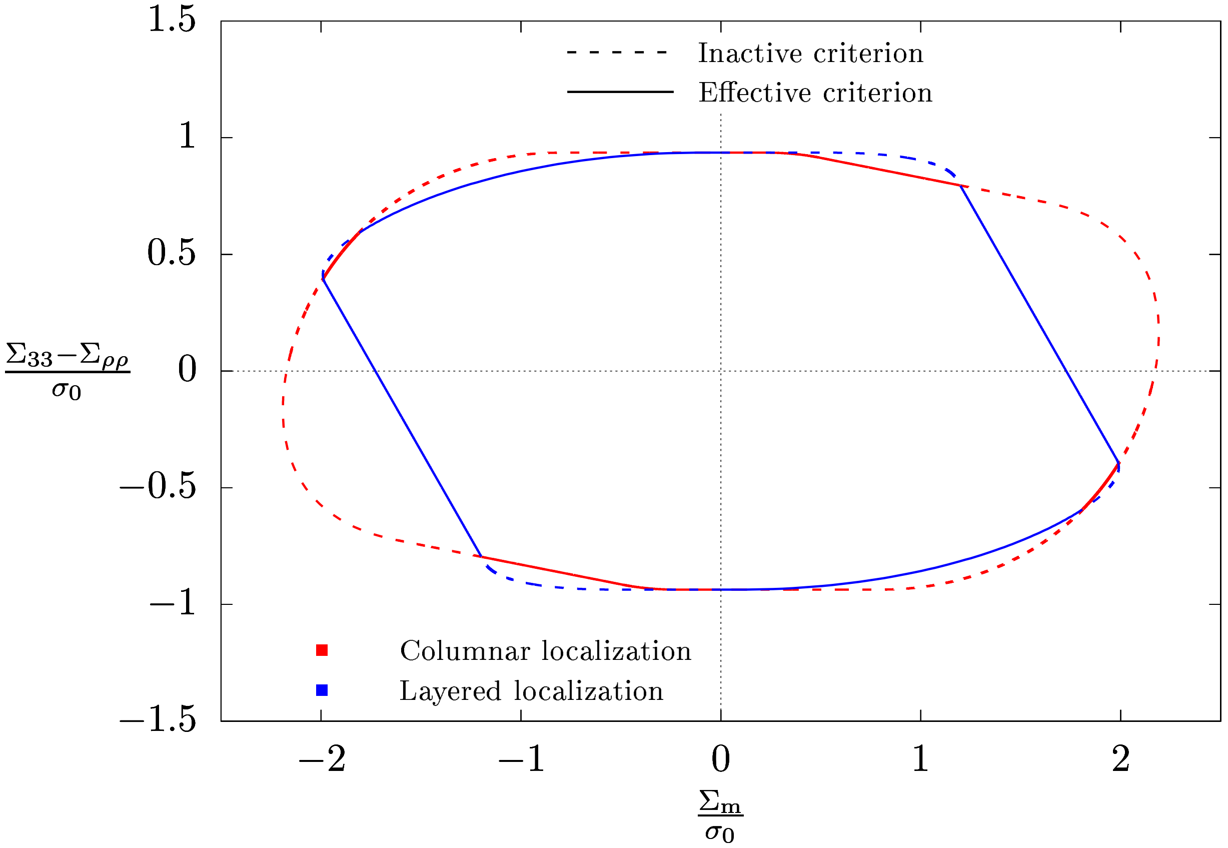

Figure 9: Total yield criterion for porous anisotropic Hill materials obtained by intersection of two individual elasticity domains associated with the criteria of Section 3.1 and 3.2. (The figure has been plotted for an isotropic material using $\chi = c = 0.4$ and $w = 1$).

In Fig. 11a,b, the assessment is performed for a material with $R_\mathrm{a} < 1$, meaning that the material is softer in the axial direction than in the transverse direction, and compared to corresponding data for an isotropic material ($R_\mathrm{a} = 1$). The final criterion accounts satisfactorily for the decrease of yield strength at the deviatoric point compared to the isotropic case, which can be traced back to the decrease of $\hat{h}_q$ (see Eq. 44_a and purple curve of Figs. 6b and 8b). The yield function also predicts correctly a larger yield stress at the hydrostatic point, meaning that the opposing effects of $\hat{h}_q$ (increasing function of R_a) and $\hat{h}_t$ (decreasing function of R_a) are correctly balanced in the analytical expressions. In Fig. 11a, the yield surface at high stress triaxialities is better approximated by the layered localization surface (notice the straight-line of slope $-3/2$ which characterizes internal necking), but as was pointed in Torki et al. (2023), two sections of the final yield surface originates from columnar localization: a larger one at dominant axial stress (columnar shielding), and a smaller one at dominant radial stress (coalescence in columns), highlighting the interest of the expression developed in Section 3.1.2. Such a conclusion is also supported by Fig. 11b in which the columnar localization surface reproduces quantitatively the numerical results for both the isotropic and the anisotropic material. The difference between isotropic and anisotropic unit-cell simulations at moderate and high triaxialities is also the confirmation that plastic anisotropy of the matrix affects significantly strain localization, both in layers and in columns.

Similar comments can be made on Fig. 11c,d (beware that axes bounds are not the same as Fig. 11a,b) which displays results for an anisotropic material with $R_\mathrm{a} > 1$. This time, the yield stress of the anisotropic material is larger than that of the isotropic material over the full yield surface. A third characteristic behavior also exists, not shown here: at values $R_\mathrm{a} \in]0.6, 1[$ close to 1, the yield surface of the anisotropic material is fully interior to that of the isotropic material: indeed, the effect of a small decrease of R_a from 1 has a stronger effect on $\hat{h}_q$ than on $\hat{h}_t$ (see Eq. 44), enabling to effectively reduce the yield stress at the hydrostatic point.

In Fig. 11e,f, the assessment is performed for anisotropic materials with different R_s. $R_\mathrm{s} = 3$ means that the matrix material is three times harder than the corresponding isotropic material when loaded in shear. It is seen that void growth yield stress is left unchanged but that coalescence is affected by the modification of R_s. Again, the criterion accounts satisfactorily for this effect, which can be linked to the increase of $\hat{h}_a$ (see Eq. 44_c and blue curve of Figs. 6b and 8b). In Fig. 11e, the yield surface at high stress triaxialities is better approximated by the surface for internal necking whereas the necklace coalescence surface reproduces quantitatively the numerical results of Fig. 11f.

From that numerical assessment, it can be concluded that plastic anisotropy has a strong effect on coalescence, whatever the pattern of strain localization, and that this effect is quantitatively captured by the yield criterion proposed in this study; depending on whether localization is columnar or in layers, the expression of Section 3.1.2 or Section 3.2.2 will be selected through the multi-criteria framework. This has been shown in the case of materials with transverse isotropy but the model is applicable to materials in which the orthotropy axes are not aligned with void axes. Full three-dimensional numerical simulations being numerically heavy and time-consuming, further numerical assessment is left for future research. Such a model has interesting outcomes for material science because it enables to quantify the effects of plastic

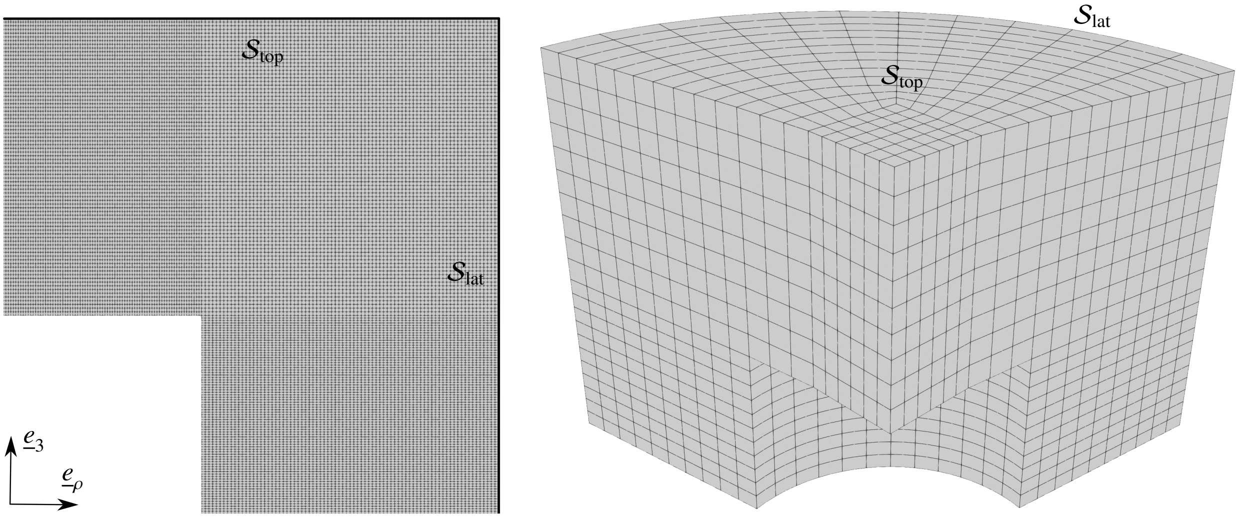

(a) (b)

Figure 10: Meshes used for numerical limit-analysis at $\chi = c = 0.4$ and $w = 1$: (a) axisymmetric mesh used for the transverse isotropy matrix; (b) one-eighth of the total mesh used for the crystal matrix.

anisotropy on ductile fracture so that materials suitable for a given application can be knowingly chosen or designed.

The criterion developed in this section is relevant for polycrystalline materials where voids are significantly larger than the grain size, so that the matrix material at the scale of the voids is composed of a large number of grains and can be described by Hill (1948) plasticity which accounts for large-scale anisotropy. However, it is well-known that voids are smaller than the grain size in many metals (Pineau et al., 2016). In these cases, each grain is a porous single crystal and this low-scale anisotropy has to be taken into account into the yield criterion, motivating the model presented in the next section.

4. Yield surface for rate-independent crystals

The second part deals with crystalline plastic anisotropy, meaning that the same unit-cell as in Section 3 is considered, this time with a single crystal matrix. A yield surface for porous single crystals under axisymmetric loading is searched by extending the previous yield criterion using the method presented in Hure (2019).

4.1. Single crystal matrix behavior

Plasticity is assumed to be related to the glide of dislocations, that can happen in a limited number of planes and directions, called crystallographic slip systems, defined by a slip plane (whose normal is along unit vector $\underline{m}_s$) and a slip direction (of unit vector $\underline{n}_s$), and represented by the following symmetric Schmid tensor : $\boldsymbol{\mu}_s = \frac{1}{2}(\underline{m}_s \otimes \underline{n}_s + \underline{n}_s \otimes \underline{m}_s)$. A face-centered cubic (FCC) material is considered, with $K = 12$ independent slips systems — the $\{111\}\langle 110\rangle$ family. Using viscoplastic regularization, the plastic strain rate writes (Hutchinson, 1976):

$$\boldsymbol{d} = \sum_{s=1}^{K} \left[\dot{\gamma}_0 \left(\frac{|\boldsymbol{\sigma} : \boldsymbol{\mu}_s|}{\tau_0} \right)^n \operatorname{sgn}(\boldsymbol{\sigma} : \boldsymbol{\mu}_s) \right] \boldsymbol{\mu}_s = \sum_{s=1}^{K} \dot{\gamma}_s \boldsymbol{\mu}_s \tag{45}$$

where τ_0 is the critical resolved shear stress (identical for all slip systems), $\dot{\gamma}_0$ a reference slip-rate (set to 1 s^{-1}) and $\dot{\gamma}_s$ the slip rate of system s. n denotes the Norton exponent: the case $n \to +\infty$ corresponds to rate-independent plasticity, which is of interest here.

The local Taylor factor associated to a single crystal subjected to a strain rate $\boldsymbol{d}$ is defined as:

$$M(\boldsymbol{d}) = \frac{\sum_{s=1}^{K} \dot{\gamma}_k \, [\boldsymbol{d}]}{d_{\mathrm{eq}}^{\mathrm{iso}}} \quad \text{with} \quad d_{\mathrm{eq}}^{\mathrm{iso}} = \sqrt{\frac{2}{3} \boldsymbol{d} : \boldsymbol{d}} \tag{46}$$

where $d_{\mathrm{eq}}^{\mathrm{iso}}$ is the von Mises equivalent deformation. In rate-independent plasticity, $(\dot{\gamma}_k)$ may be determined from $\boldsymbol{d}$ as the set that verifies $\sum \dot{\gamma}_s \boldsymbol{\mu}_s = \boldsymbol{d}$ while minimizing $\sum |\dot{\gamma}_s|$, as suggested by Taylor (1938). Since this problem is a minimization under linear hard constraints involving inequalities, it can be solved through classical algorithms of linear programming (see Van Houtte (1988) for this specific case). Through the set of Schmid tensors $(\boldsymbol{\mu}_s)$, M is strongly dependent on the crystallographic orientation. This value is of great interest for our study since, in a single crystal, the microscopic plastic dissipation writes:

$$\sup_{\boldsymbol{\sigma}^* \in \mathscr{C}} \boldsymbol{\sigma}^* : \boldsymbol{d} = \sum_k \tau_0 \dot{\gamma}_k = M(\boldsymbol{d}) \tau_0 d_{\mathrm{eq}}^{\mathrm{iso}} \tag{47}$$

Eq. 47 can then be used to re-apply the limit analysis framework of Section 3 considering $\sigma_0 = M(\boldsymbol{d})\tau_0$.

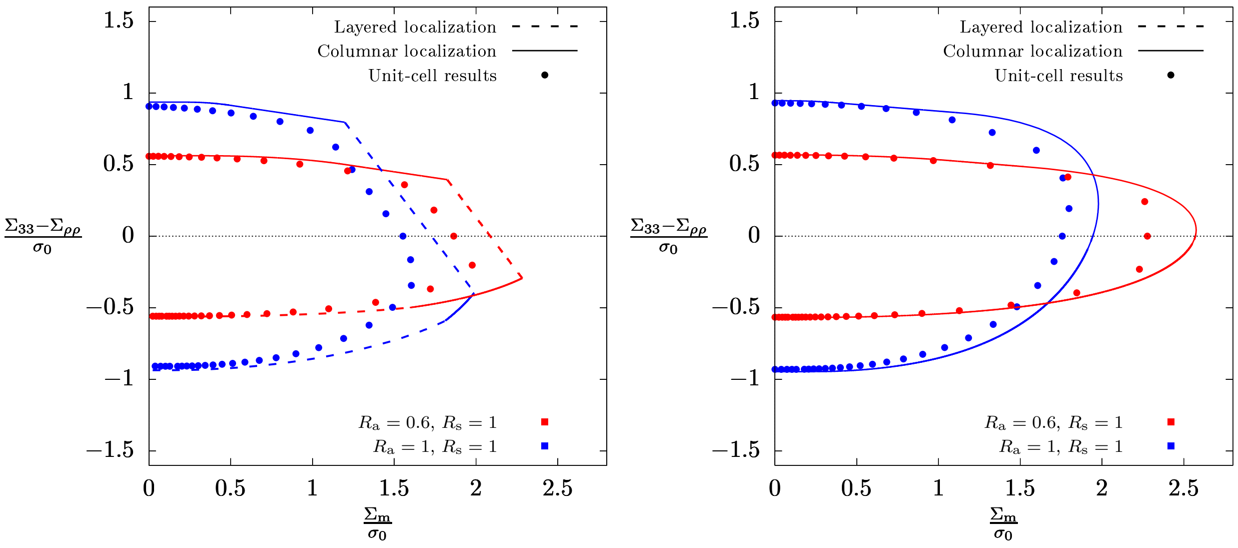

(a) $\chi = 0.4$, $c = 0.4$

(b) $\chi = 0.3$, $c = 0.6$

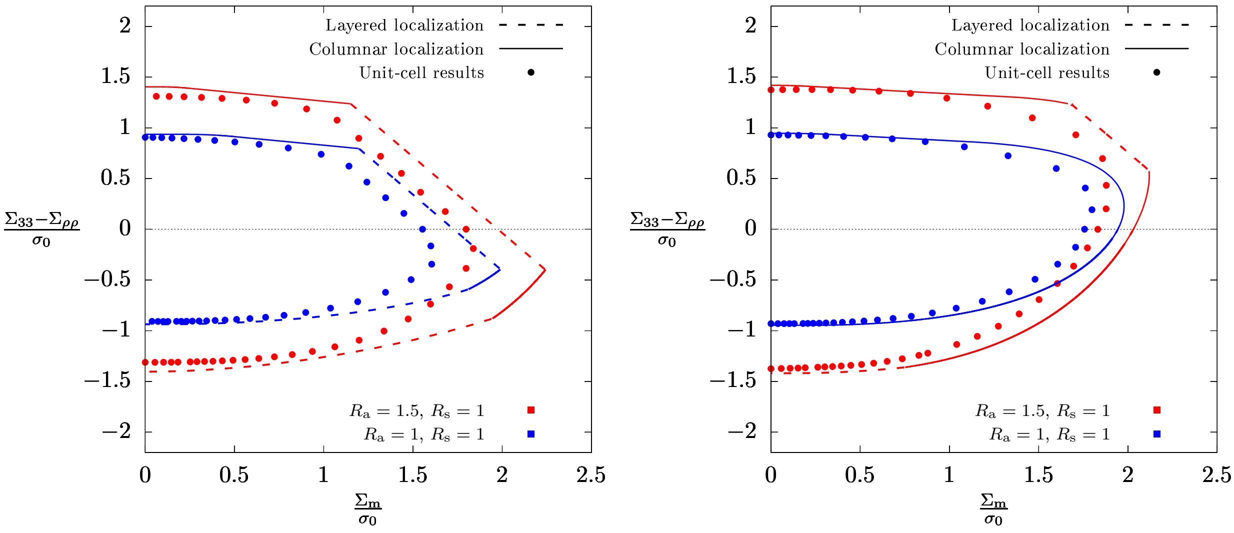

(c) $\chi = 0.4$, $c = 0.4$

(d) $\chi = 0.3$, $c = 0.6$

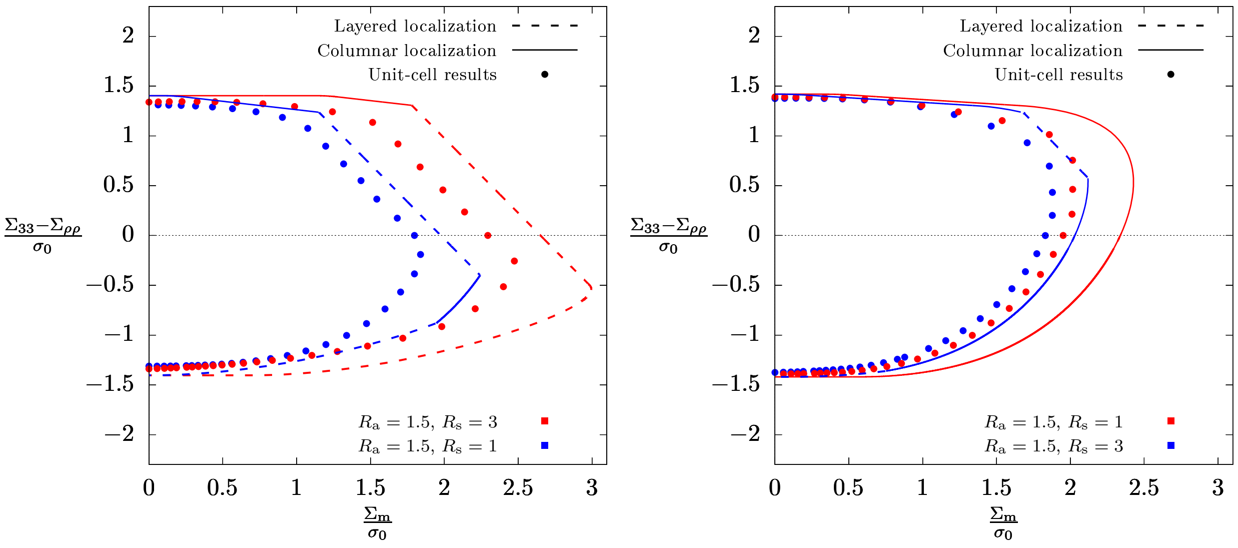

(e) $\chi = 0.4$, $c = 0.4$

(f) $\chi = 0.3$, $c = 0.6$

Figure 11: Comparison between the numerical limit-analysis (points) and the analytical criterion (columnar localization shown with full lines and layered localization drawn with dashed lines) for a set of transverse isotropic materials defined by yield stress ratios R_{a} and R_{s}. Two void geometries are considered: (a,c,e) $\chi = 0.4$, $c = 0.4$, $w = 1$; (b,d,f) $\chi = 0.3$, $c = 0.6$, $w = 1$.

4.2. Approximate macroscopic dissipation

At the macroscopic scale, the following approximation can be performed on a volume A:

$$\Pi^{(\mathrm{A})} = \frac{1}{|\Omega|}\int_{\Omega_\mathrm{A}} M(\boldsymbol{d})\tau_0 d^{\mathrm{iso}}_{\mathrm{eq}} \approx \left(\frac{1}{|\Omega_\mathrm{A}|}\int_{\Omega_\mathrm{A}} M(\boldsymbol{d})\right)\left(\frac{1}{|\Omega|}\int_{\Omega_\mathrm{A}} \tau_0 d^{\mathrm{iso}}_{\mathrm{eq}}\right) = \left(\frac{1}{|\Omega_\mathrm{A}|}\int_{\Omega_\mathrm{A}} M(\boldsymbol{d})\right)\Pi^{(\mathrm{A})}_{\mathrm{iso}} \tag{48}$$

with $\Pi^{(\mathrm{A})}_{\mathrm{iso}}$ the corresponding dissipation in an equivalent isotropic material of uniaxial yield stress τ_0. Additional details can be found in Hure (2019). Supposing that the velocity field given in Torki et al. (2023) for columnar localization in isotropic material can be used to describe approximately the same localization mode in crystals, Eq. 48 is successively applied to the three zones of the unit-cell (plugs, matrix and interface), leading to:

$$\Pi \approx \underbrace{\left(\frac{1}{2\pi}\int_0^{2\pi} M\left(\boldsymbol{d}^{(\mathrm{I})},\theta\right)\,\mathrm{d}\theta\right)}_{M_1}\Pi^{\mathrm{surf}}_{\mathrm{iso}} + \underbrace{\left(\frac{1}{\pi(1-\chi^2)}\int_\chi^1\int_0^{2\pi} M\left(\boldsymbol{d}^{(\mathrm{M})},\rho,\theta\right)\rho\,\mathrm{d}\theta\,\mathrm{d}\rho\right)}_{M_2(\chi,\xi)}\Pi^{(\mathrm{M})}_{\mathrm{iso}} + \underbrace{\left(\frac{1}{2\pi}\int_0^{2\pi} M\left(\boldsymbol{d}^{(\mathrm{P})},\theta\right)\,\mathrm{d}\theta\right)}_{M_4}\Pi^{(\mathrm{P})}_{\mathrm{iso}} \tag{49}$$

where $\boldsymbol{d}^{(\mathrm{M})}$ and $\boldsymbol{d}^{(\mathrm{P})}$ are given by Eq. 14, and $\boldsymbol{d}^{(\mathrm{I})}$ can be found in the text between Eq. 5. Expressions for $\Pi^{(\mathrm{M})}_{\mathrm{iso}}$, $\Pi^{(\mathrm{P})}_{\mathrm{iso}}$ and $\Pi^{\mathrm{surf}}_{\mathrm{iso}}$ are obtained by specializing Eqs. 19 and 20 with $\hat{h}_q = \hat{h}_t = \hat{h}_a = 1$ and $\sigma_0 = \tau_0$. The dependence of M_1, M_2 and M_4 on loading and geometry have been established by keeping in mind that $M(\boldsymbol{d})$ is homogeneous of degree 0, *i.e.* colinear strain rates tensors share the same Taylor factor. Note that the present M_1 is equal to the M_1 defined in Hure (2019), and that $M_2(\chi)$ of the aforementioned paper corresponds to $M_2(\chi, 1)$ of the present study. It is also easily seen that $M_2(0,\chi) = M_4$.

Similarly, the macroscopic dissipation associated with the trial field of Morin et al. (2016a) can be approximated by:

$$\Pi \approx \underbrace{\left(\frac{1}{2\pi}\int_0^{2\pi} M\left(\boldsymbol{d}^{(\mathrm{I})},\theta\right)\,\mathrm{d}\theta\right)}_{M_1}\Pi^{\mathrm{surf}}_{\mathrm{iso}} + \underbrace{\left(\frac{1}{\pi(1-\chi^2)}\int_\chi^1\int_0^{2\pi} M\left(\boldsymbol{d}^{(\mathrm{L})},\rho,\theta\right)\rho\,\mathrm{d}\theta\,\mathrm{d}\rho\right)}_{M_2\left(\chi,\frac{\xi}{\bar{\xi}}\right)}\Pi^{(\mathrm{L})}_{\mathrm{iso}} + \underbrace{\left(\frac{1}{2\pi}\int_0^{2\pi} M\left(\boldsymbol{d}^{(\mathrm{S})},\theta\right)\,\mathrm{d}\theta\right)}_{M_4}\Pi^{(\mathrm{S})}_{\mathrm{iso}} \tag{50}$$

On the one hand, the dependence of M_2 on χ is rather weak, as seen in Fig. 12a for a handful of crystal orientations defined in Table 1. Therefore, as already suggested in Sénac et al. (2022), it is discarded and M_2 is evaluated for $\chi = 0.3$, since it is usually preferable to predict correctly the beginning of localization rather than the later stages. On the other hand, the dependence of M_2 on ξ is quite significant, as shown in Fig. 12b. Thus, the ξ-derivative of M_2 cannot be neglected in the determination of yield surfaces and will be denoted M_2'. It is also worthy to notice that M_2 is not a perfectly even function of ξ, the slight difference being attributable to the constant terms in $\boldsymbol{d}^{(M)}$.

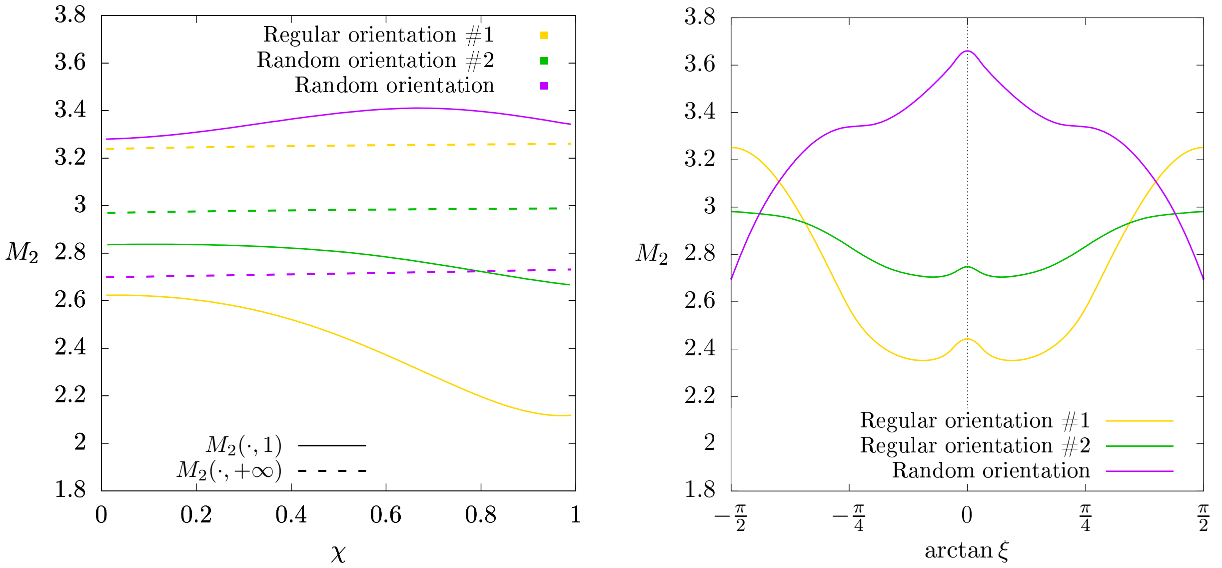

(a)

(b)

Figure 12: Average Taylor factor M_2 for various crystal orientations: (a) effect of χ at fixed $\xi \in \{1, +\infty\}$; (b) effect of ξ for fixed $\chi = 0.3$.

Table 1: Definition of the crystallographic orientations. Euler angles are given using Bunge convention; Miller indexes define loading axes in the crystal frame.

#		Euler angles			Miller indexes	
	ϕ_1 (°)	Φ (°)	ϕ_2 (°)	$\underline{e}_1$	$\underline{e}_2$	$\underline{e}_3$
● Regular orientation #1	0	0	0	[100]	[010]	[001]
● Regular orientation #2	90	24.09	333.43	$[1\bar{2}1]$	[210]	$[\bar{1}25]$
● Random orientation	93.48	53.17	315.41			

4.3. Yield surface

As shown in Appendix A, two tangent surfaces can be derived from the approximated expressions of the macroscopic potential given in the previous section. However, these *Taylor surfaces* present two major limitations: first, the use of Eqs. 49 and 50 offers no guarantee on the convexity of Π so the convexity of Taylor surfaces cannot be assured; then, they require the computation of M_2 and its derivative for each crystallographic orientation, which is quite cumbersome. Thus, a pragmatic approach consists in identifying an equivalent Hill porous material whose two individual yield surface are close to the Taylor surfaces of the porous single crystal. As seen in Section 3, each individual yield surface (either columnar localization or layered localization) of porous Hill material is characterized by three factors: $\hat{h}_a$, $\hat{h}_t$ and $\hat{h}_q$.

Since it has been noticed on Figs. 6b and 8b that the effects of $\hat{h}_a$ and $\hat{h}_t$ on the shape of yield surfaces are almost impossible to distinguish, $\hat{h}_a$ is arbitrarily fixed to 0 to reduce the number of freedom degrees. Then, $\hat{h}_t$ and $\hat{h}_q$ are chosen so that the flat parts of the Taylor surface and the flat parts of porous Hill material yield surface coincide. For both columnar and layered localization, the equality of the deviatoric point of the yield surface (either Eq. 27_b or 38_b) and that of the Taylor surface (either Eq. A.2_b or Eq. A.5_b) yields:

$$\sqrt{\hat{h}_q} = M_4 \tag{51}$$

Then, in the case of the layered localization, identifying the internal necking stresses of both surfaces (Eq. 39_b and Eq. A.6_b) leads to:

$$\sqrt{\frac{\hat{h}_t^{\mathrm{l}}}{3}}\mathcal{A}\left(\frac{1}{M_4}\sqrt{\frac{\hat{h}_t^{\mathrm{l}}}{3}}\right) + M_4\mathcal{B}\left(\frac{1}{M_4}\sqrt{\frac{\hat{h}_t^{\mathrm{l}}}{3}}\right) = M_2(1)\left[\frac{1}{\sqrt{3}}\mathcal{A}\left(\frac{1}{\sqrt{3}}\right) + \mathcal{B}\left(\frac{1}{\sqrt{3}}\right)\right] + M_1\frac{\chi^3 - 3\chi + 2}{3\sqrt{3}w\chi} \tag{52}$$

Similarly, in the case of columnar localization, identifying the columnar shielding stresses of both surfaces (Eq. 29_b and Eq. A.3_b) leads to:

$$\sqrt{\frac{\hat{h}_t^{\mathrm{c}}}{3}}\chi^2\mathcal{A}\left(\frac{\chi^2}{M_4}\sqrt{\frac{\hat{h}_t^{\mathrm{c}}}{3}}\right) + M_4\mathcal{B}\left(\frac{\chi^2}{M_4}\sqrt{\frac{\hat{h}_t^{\mathrm{c}}}{3}}\right) = M_2(\chi^2)\left[\frac{\chi^2}{\sqrt{3}}\mathcal{A}\left(\frac{\chi^2}{\sqrt{3}}\right) + \mathcal{B}\left(\frac{\chi^2}{\sqrt{3}}\right)\right] + M_1\frac{w}{\sqrt{3}}\frac{(1-c)^2}{c}\chi^2 \tag{53}$$

Eqs. 52 and 53 respectively constitute implicit definitions of function $\hat{h}_t^{\mathrm{l}}(M_1, M_2(1), M_4, \chi, w)$ and function $\hat{h}_t^{\mathrm{c}}(M_1, M_2(\chi^2), M_4, \chi, c, w)$. Obviously, $\hat{h}_t^{\mathrm{c}}$, corresponding to columnar localization, will be different from $\hat{h}_t^{\mathrm{l}}$, related to layered localization. For FCC crystals, it can be assessed numerically that the dependence of $\hat{h}_t$ on the crystal orientation is weak compared to its dependence on void parameters. Thus, the crystallographic dependence of $\hat{h}_t$ can be ignored. As a consequence, $\hat{h}_t$ are evaluated for each set of (χ, c, w) through Eqs. 52-53 by replacing Taylor factors by their mean values:

$$\langle M_1\rangle \approx 3.197\ ,\quad \langle M_2(1)\rangle \approx 2.806\ ,\quad \left\langle M_2(\chi,\chi^2)\right\rangle \approx \begin{cases} 2.884 & (\chi = 0.3) \\ 2.845 & (\chi = 0.4) \\ 2.775 & (\chi = 0.6) \end{cases}\ ,\quad \langle M_4\rangle \approx 2.929 \tag{54}$$

For instance, the values of $\hat{h}_q$, $\hat{h}_t^{\mathrm{c}}$ and $\hat{h}_t^{\mathrm{l}}$ are given in Table 2 for the three crystallographic orientations of Table 1 and two void geometries with $w = 1$: on the one hand, $\chi = c = 0.4$, and on the other hand $\chi = 0.3$ and $c = 0.6$.

Table 2: Anisotropy factors of the equivalent yield surfaces for porous single crystal.

Crystal	● Regular orientation #1	● Regular orientation #2	● Random orientation
$\sqrt{\hat{h}_q}$	2.45	2.76	3.67
Void geometry		$\chi = c = 0.4$	$\chi = 0.3$, $c = 0.6$
	$\sqrt{\hat{h}_t^{\mathrm{c}}}$	6.13	3.03
	$\sqrt{\hat{h}_t^{\mathrm{l}}}$	3.97	4.19

As in the case of porous Hill materials, the final predicted yield criterion for porous single crystals is given by the intersection of the equivalent surfaces corresponding to columnar localization and layered localization.

4.4. *Numerical assessment*

In this section, the numerical assessment of the criterion defined in the previous section is conducted on a set of three crystallographic orientations given in Table 1.

In order to assess the predicted yield criterion, numerical limit-analysis is conducted with `Cast3M` for the aforementioned crystallographic orientations. Crystal elasticity is chosen to obey an isotropic Hooke law of Young modulus $Y = 10^3$ MPa and Poisson ratio $\nu = 0.49$. As stated before, results presented in the following do not depend on these values. In the following, the value $n = 100$ is chosen in Eq. 45 to ensure that crystal behavior is quasi-rate-independent. Since transverse isotropy is no longer verified, the full unit-cell has to be meshed; one-eighth of the mesh is shown in Fig. 10b. Note that due to the computational burden associated with three-dimensional computations, the mesh is coarser (20400 quadratic elements with reduced integration) than in Fig. 10a. Still, it was checked for convergence against a similar mesh of 160000 elements: the relative error was found to be below 1%.

The boundary conditions are consistent with the axisymmetric case, described in Section 3.3: the radial displacement is homogeneous along the lateral exterior surface of the unit-cell, the axial displacements are homogeneous on the top and the bottom surface (with opposite signs) and the angular displacement is set to 0 on the whole exterior surface. Note that no rigid-body motion can occur with these conditions. As in the previous part, the ratio of axial displacement on radial displacement is continuously adjusted in the Newton-Raphson iterations to reach the prescribed macroscopic stress ratio $\Sigma_{\rho\rho}/\Sigma_{33}$.

The quality of the criterion is checked against numerical limit analysis simulations in Fig. 13. Given the fact that trial velocity fields used in Section 4.2 were originally designed for isotropic materials, they diverge significantly from the real velocity fields and therefore cannot be expected to be tight upper bounds for the macroscopic dissipation. In an effort to acknowledge this gap, the predicted criterion plotted in Fig. 13 is scaled down in order to recover the best possible agreement at the deviatoric point:

$$\left(\Sigma_\mathrm{m}, \Sigma_\mathrm{eq}\right)_\mathrm{model} = q \cdot \left(\Sigma_\mathrm{m}, \Sigma_\mathrm{eq}\right)_\mathrm{analytical} \tag{55}$$

where the analytical model is constituted from the expressions of Sections 3.1.2 and 3.2.2 used with anisotropy values from Table 2 and where $q = 0.85$ is a single calibration parameter.

Comparisons between the ensuing yield surface and the numerical surface are shown in Fig. 13 for two different void parameters: $\chi = c = 0.4$ (left-hand side), and $2\chi = c = 0.6$ (right-hand side); w is set to 1 in both cases. Despite the strong influence of crystal orientation on plastic yielding, the displayed agreement is quite satisfying. First, the characteristic sections of coalescence in columns, internal necking and columnar shielding are well visible in the numerical surfaces, which justifies qualitatively the approach used in Section 4.3. Then, the effect of crystallographic orientations is well accounted for: note that the rankings of deviatoric yield stress are identical for numerical and predicted surfaces (this can be seen on all subgfigures of Fig. 13), and the same can be said about internal necking yield stress (see Fig. 13a,b,c). Overall, the quantitative predictions are of similar quality compared to those observed in Section 3.3 for porous Hill materials.

5. Homogenized model for porous Hill materials

Prediction of yield surfaces for porous materials is only the first step in the modeling of ductile fracture. As a matter of fact, microstructure parameters evolve under plastic flow, gradually modifying the yield surface. Accounting for this coupling is of paramount importance to predict the behavior of materials until failure, and therefore to estimate ductility. Thus, the yield criterion must be supplemented with evolution laws for the microstructure. Various homogenized models of ductile fracture combining void growth and coalescence in layers have been proposed in the literature for isotropic materials (Benzerga and Leblond, 2010; Keralavarma, 2017; Torki and Benzerga, 2018a; Vishwakarma and Keralavarma, 2019; Reddi et al., 2019; Keralavarma et al., 2020; Torki et al., 2021; Torki and Benzerga, 2022) as well as porous single crystals (Scherer et al., 2021; Sénac et al., 2022) but none of them include coalescence in columns.

5.1. *Sequential limit analysis*

In the following, the evolution under plastic flow of the unit-cell shown in Fig. 3 with a Hill matrix is studied under the assumption that both the void and the unit-cell remain cylindrical. Thus, the four geometry parameters that define microstructure are R, H, r and h. Boundary conditions are such that $\dot{H} = D_{33}H$ and $\dot{R} = D_{\rho\rho}R$, leaving two unknown evolution laws for r and h, or, alternatively for χ and c. Therefore, the mere application of the incompressibility of the matrix material cannot close the equations and an additional hypothesis is needed. In Gurson's analysis, spherical invariance was such an hypothesis; in the approach of internal necking by Thomason (1985), the rigid character the upper and lower zones provided an additional constraint, as well as in coalescence under combined tension and shear (Torki et al., 2017; Torki and Benzerga, 2018a,b). In the present case, none of these hypotheses are acceptable. Therefore, it is resorted to sequential limit analysis (Leblond et al., 2018), *i.e.* the trial velocity fields given by Eqs. 12 and 30 will be used to derive evolution equations of the microstructure. In that framework, $\dot{r} = v_\rho^{(\mathrm{M})}(r, z)$ and $\dot{h} = v_z^{(\mathrm{P})}(\rho, h)$.

On the one hand, for the trial velocity field corresponding to columnar localization, it leads to:

$$\dot{c} = \frac{\dot{h}}{H} - \frac{\dot{H}h}{H^2} = \frac{1-c}{\chi^2}D_{kk} \quad , \quad \dot{\chi} = \frac{\dot{r}}{R} - \frac{\dot{R}r}{R^2} = \frac{1}{2}\left(\frac{1}{\chi} - \chi\right)D_{kk} \quad , \quad \dot{w} = \frac{\dot{h}}{r} - \frac{\dot{r}h}{r^2} = \frac{w}{\chi^2}\left(\frac{1}{c} - \frac{3}{2}\right)D_{kk} + \frac{3}{2}wD_{33} \tag{56}$$

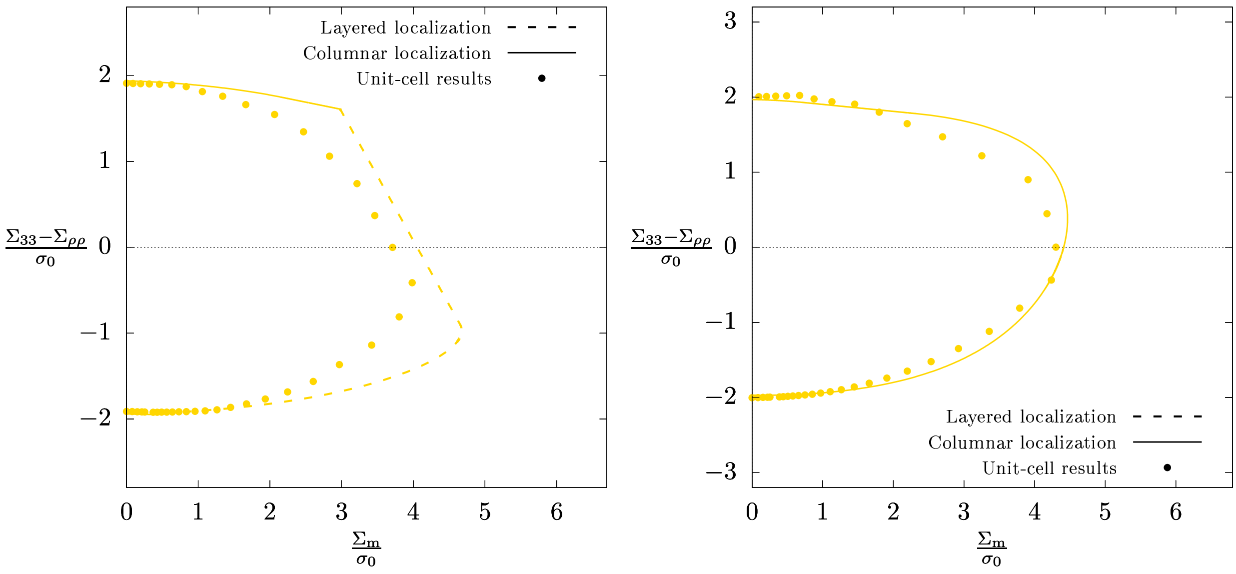

(a) χ = 0.4, c = 0.4, regular orientation #1 (b) χ = 0.3, c = 0.6, regular orientation #1

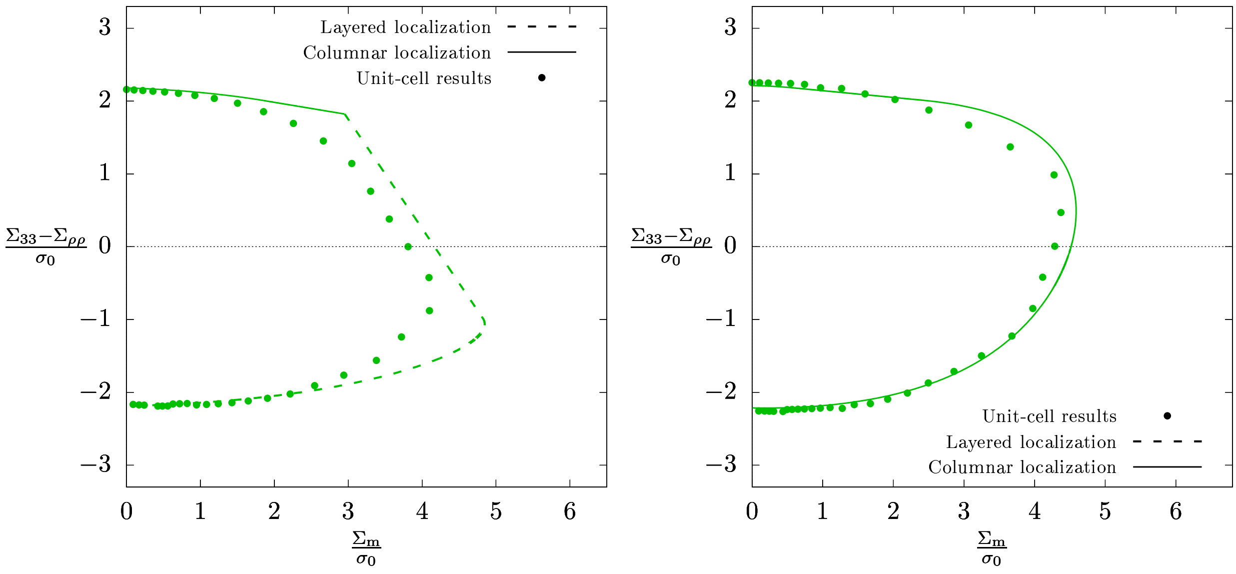

(c) χ = 0.4, c = 0.4, regular orientation #2 (d) χ = 0.3, c = 0.6, regular orientation #2

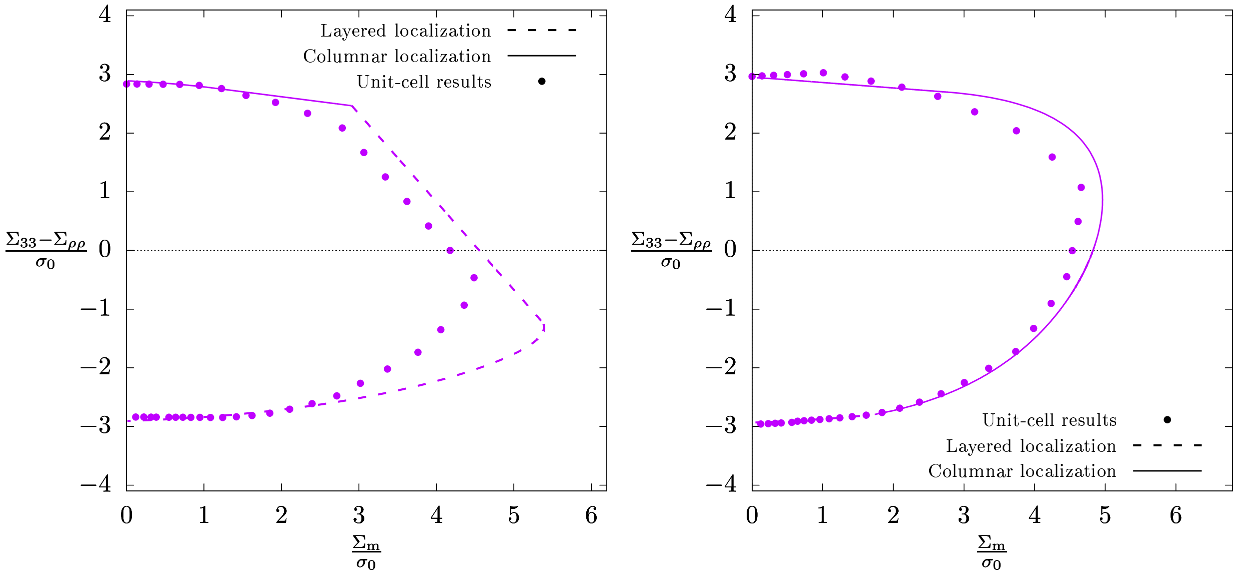

(e) χ = 0.4, c = 0.4, random orientation (f) χ = 0.3, c = 0.6, random orientation

Figure 13: Comparison between the numerical limit-analysis (points) and the calibrated analytical criterion, with its sections of columnar localization (full lines) and layered localization (dashed lines) for a set of porous single crystals. Two void geometries are considered: (a,c,e) χ = 0.4, c = 0.4, w = 1; (b,d,f) χ = 0.3, c = 0.6, w = 1.

On the other hand, for the trial velocity field corresponding to layered localization, sequential limit-analysis yields:

$$\dot{c} = (1-c)D_{kk} \quad , \quad \dot{\chi} = \frac{1}{2c}\left(\frac{1}{\chi} - \chi\right)D_{kk} \quad , \quad \dot{w} = \frac{w}{2}\left[3\left(\frac{1}{c} - 1\right) - \frac{1}{c\chi^2}\right]D_{kk} + \frac{3}{2}wD_{33} \tag{57}$$

Note that Eqs. 57 are an extension of the evolution laws for λ, χ and w given by Benzerga and Leblond (2010) in the case $\gamma = \frac{1}{3}$. The incompressibility condition of the matrix writes

$$\frac{\partial}{\partial t}\left[2\pi HR^2 - 2\pi hr^2\right] = HR^2\left[D_{kk}(1 - c\chi^2) - \chi^2\dot{c} - 2c\chi\dot{\chi}\right] = 0 \tag{58}$$

and is compatible with Eqs. 56 and 57, which is no surprise since trial velocity fields were chosen to verify incompressibility of the matrix material.

The homogenized model for Hill porous materials is the combination of the multi-surface yield criterion obtained previously (see Sections 3.1.2 and 3.2.2) along with the corresponding evolution laws (respectively Eqs. 56 and 57). The set of microstructure equations to be applied is chosen according to the stress criterion currently activated. The issue of surface intersections can be solved by combining criteria using a viscoplastic framework such as the one used in Sénac et al. (2022) or a perfect plastic framework following Koiter (1953). Note that since the matrix deform during ductile fracture, evolution equations for orthotropy axes of the matrix are also needed. However, given the absence of macroscopic shear in the axisymmetric loadings considered here, it will be supposed that these axes do not rotate significantly.

5.2. Discussion

Evolution laws do not benefit from the variational framework associated with classical limit analysis (Eq. 4), and thus Eqs. 56 and 57 have no guarantee of holding unless the trial velocity field is very close from the real field. Besides, spatial inhomogeneities of the velocity field on the void surface can also lead to evolution of the void towards shapes that are no longer cylindrical (see for instance Keralavarma et al. (2011), Morin et al. (2016b) and Hosseini et al. (2022) for the same issue with ellipsoidal cavities), which would reduce the predictive capability of the model. Finally, since the chosen trial fields do not depend on material anisotropy, they result in evolution laws that are also independent from it, providing that the strain rate is fixed; this simplifying hypothesis needs to be assessed.

Numerical velocity fields for various plastic anisotropy are presented in Fig. 14 in the case where $\chi = 0.3$ and $c = 0.6$ for two displacement boundary conditions. For an isotropic material, they correspond to two different deformation modes: columnar shielding ($D_{33} = -D_{\rho\rho} = 1$, see Fig. 14a) and coalescence in columns ($D_{\rho\rho} = -2D_{33} = 1$, see Fig. 14b). On the one hand, the velocity field for the first loading condition remains the same for anisotropic materials (Fig. 14c,e), except for the material with lower axial strength (Fig. 14b) where slight deviations arise: notice that the plugs are no longer shielded from plasticity. On the other hand, the velocity field associated with the second loading condition seems more sensible to anisotropy as the material with $R_{\mathrm{s}} = 3$ deviates strongly from the isotropic field while the material with $R_{\mathrm{a}} = 0.6$ displays reduced velocity magnitude in the plugs. The influence of anisotropy on internal necking is studied in Fig. 15 at $\chi = 0.4$ and $c = 0.4$. The velocity field is found to be quite stable when varying plastic anisotropy: compare the isotropic field (Fig. 15a) to the anisotropic field that displays the strongest deviations from it (Fig. 15b).

The conclusion to be drawn from these comparisons is the following: supposing that evolution laws are accurate enough to model damage evolution in the isotropic material, the velocity field mismatches highlighted in the case of coalescence in columns (right-hand side of Fig. 14) would require a correction depending on material anisotropy to account satisfactorily for microstructure evolution. Such a correction seems to be less necessary in the case of columnar shielding (left-hand side of Fig. 14) and useless in the case of internal necking (Fig. 15).

A sense of the accuracy of evolution laws obtained by sequential limit analysis can be obtained by comparing the velocity field obtained by numerical limit-analysis in the isotropic material and the trial fields used in the theoretical analysis. When velocity fields are compared *at equal displacement boundary conditions* (*i.e.* fixed ξ), the result is rather disappointing. Indeed, as seen in Fig. 16a, the trial velocity field predicts coalescence in columns instead of columnar shielding (Fig. 14a), and the coalescence in columns of Fig. 16b misses the fact that the void lateral surface moves faster than the unit-cell lateral surface (see Fig. 14b). These discrepancies are likely to result in inaccurate evolution for internal parameters. However, when numerical velocity fields are compared *at equal stress triaxialities*, the picture is completely different. This time, columnar shielding is correctly predicted (Fig. 16c), and the void surface moves faster that the unit-cell exterior surface (Fig. 16d). In Fig. 16d, it is also visible that the ratio of the void upper surface axial velocity on the lateral surface radial velocity is more coherent with numerical fields (right-hand side of Fig. 14) than that of Fig. 16b. Finite strain unit-cell computations at fixed stress triaxiality ratios would be needed for definitive assessment of evolution laws obtained by sequential limit-analysis (Eqs. 56 and 57) but these simulations are left for future research. In finite-element computations, mechanical solving at material points couples stress and displacement conditions, so the resulting velocity fields might lie between those obtained using pure boundary conditions. This observation is yet another remainder that a satisfying analytical yield surface must approximate correctly yield stresses as well as their derivatives (*e.g.* Leblond and Morin (2014)).

Assuming for now that Eq. 56 are a good approximation of microstructure evolution during necklace coalescence, they can be invoked to explain the observations of Benzerga (2002) and Benzerga et al. (2004a) which reported coalescence in columns occurring between close-packed prolate cavities. Torki et al. (2023) have put forward that at fixed unit-cell aspect ratio λ, increasing w contracts the yield surface and therefore favors coalescence in columns; however, at fixed c and χ, increasing w hinders necklace coalescence (see Fig. 6a) and fosters internal necking (see Fig. 8a). Thus, one cannot say

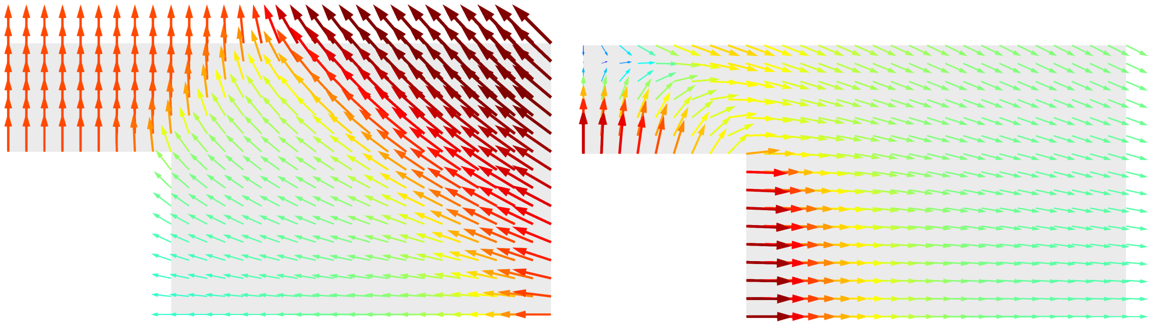

(a) $R_\mathrm{a} = R_\mathrm{s} = 1$, $D_{33} = -D_{\rho\rho} = 1$, $\Sigma_{\rho\rho}/\Sigma_{33} = -0.668$ (b) $R_\mathrm{a} = R_\mathrm{s} = 1$, $D_{\rho\rho} = -2D_{33} = 1$, $\Sigma_{\rho\rho}/\Sigma_{33} = 1.636$

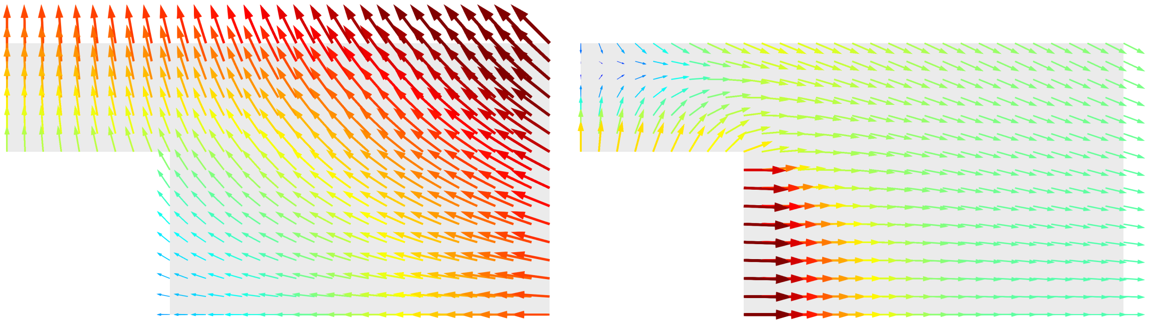

(c) $R_\mathrm{a} = 0.6$, $R_\mathrm{s} = 1$, $D_{33} = -D_{\rho\rho} = 1$, $\Sigma_{\rho\rho}/\Sigma_{33} = -0.678$ (d) $R_\mathrm{a} = 0.6$, $R_\mathrm{s} = 1$, $D_{\rho\rho} = -2D_{33} = 1$, $\Sigma_{\rho\rho}/\Sigma_{33} = 1.098$

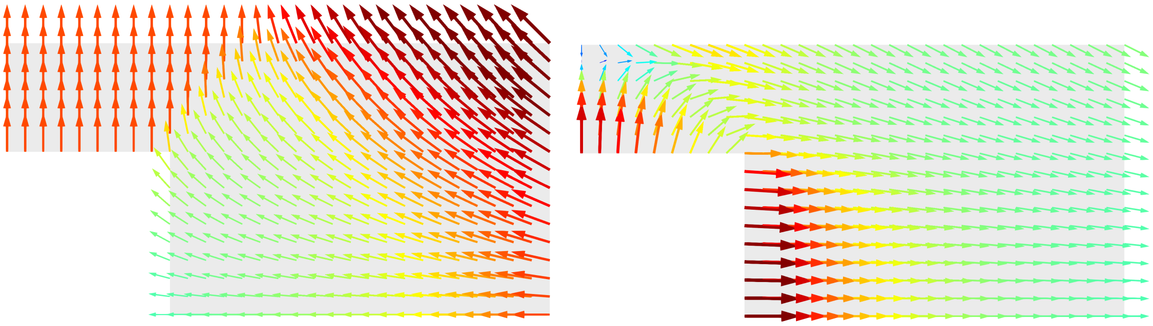

(e) $R_\mathrm{a} = 1.5$, $R_\mathrm{s} = 1$, $D_{33} = -D_{\rho\rho} = 1$, $\Sigma_{\rho\rho}/\Sigma_{33} = -0.235$ (f) $R_\mathrm{a} = 1.5$, $R_\mathrm{s} = 1$, $D_{\rho\rho} = -2D_{33} = 1$, $\Sigma_{\rho\rho}/\Sigma_{33} = 3.437$

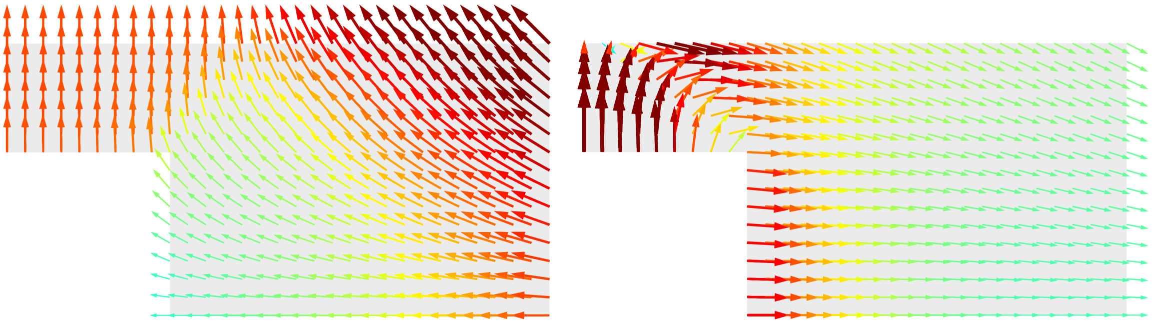

(g) $R_\mathrm{a} = 1.5$, $R_\mathrm{s} = 3$, $D_{33} = -D_{\rho\rho} = 1$, $\Sigma_{\rho\rho}/\Sigma_{33} = -0.403$ (h) $R_\mathrm{a} = 1.5$, $R_\mathrm{s} = 3$, $D_{\rho\rho} = -2D_{33} = 1$, $\Sigma_{\rho\rho}/\Sigma_{33} = 3.030$

Figure 14: Comparison of the numerical kinematic limit analysis velocity fields for $\chi = 0.4$, $c = 0.6$, $w = 1$, corresponding to $D_{33} = -D_{\rho\rho} = 1$ (left row) or $D_{\rho\rho} = -2D_{33} = 1$ (right row). Different ratios R_a and R_s are presented.

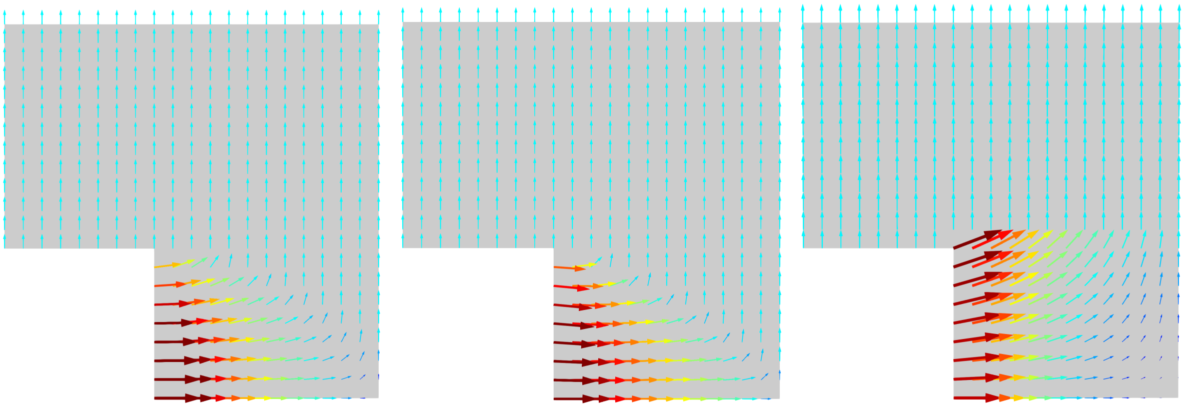

(a) $R_a = R_s = 1$, $D_{\rho\rho} = 0$ (b) $R_a = 1.5$, $R_s = 1$, $D_{\rho\rho} = 0$ (c) Trial velocity field, $D_{\rho\rho} = 0$

Figure 15: Numerical limit-analysis velocity fields and trial velocity field (Eq. 30) for $\chi = 0.4$, $c = 0.4$, $w = 1$.

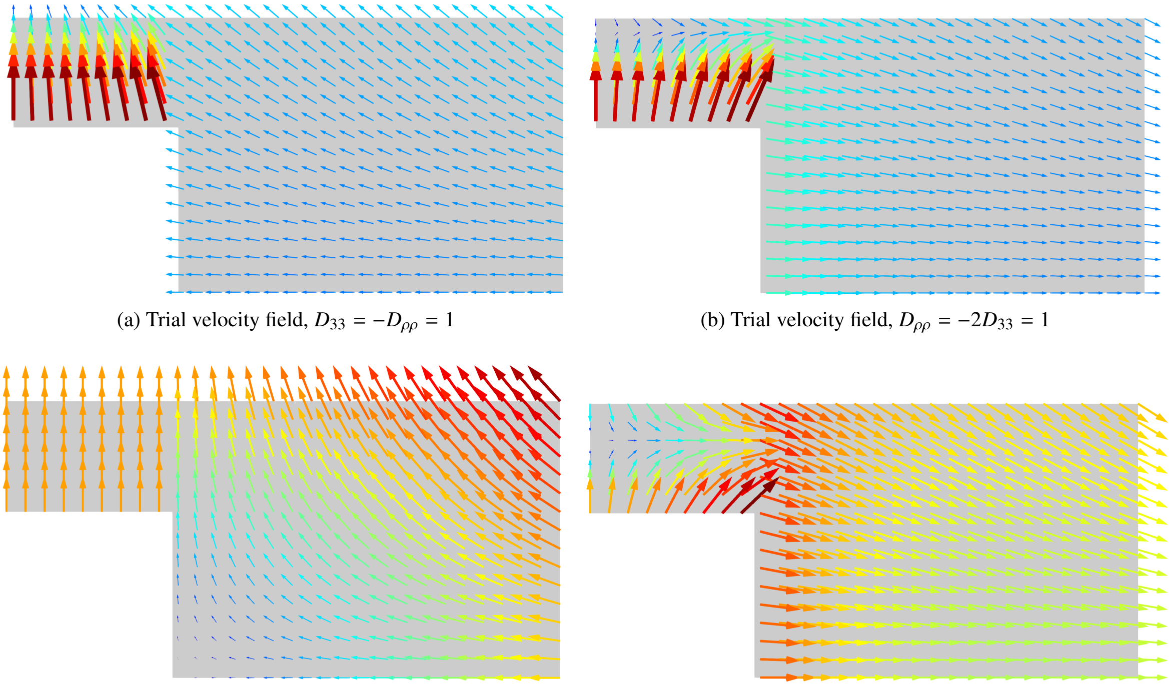

(a) Trial velocity field, $D_{33} = -D_{\rho\rho} = 1$

(b) Trial velocity field, $D_{\rho\rho} = -2D_{33} = 1$

(c) Trial velocity field, $\Sigma_{\rho\rho}/\Sigma_{33} = -0.668$

(d) Trial velocity field, $\Sigma_{\rho\rho}/\Sigma_{33} = 1.636$

Figure 16: Trial velocity field of Eq. 12 for $\chi = 0.4$, $c = 0.6$, $w = 1$.

that necklace coalescence *occurs* preferentially for prolate cavities; in fact, tensile necklace coalescence *produces* prolate cavities. This observation arises from Eq. 56_c: for $c \leq \sqrt{2/3}$ and $D_{kk} > 0$, coalescence in columns leads to very significant increase of w. From Eq. 56_a, it also inferred that tensile coalescence in columns is a self-sustaining phenomenon since $\dot{c} > \dot{\chi}$ for c verifying the following inequality:

$$c \leq 1 - \frac{1}{2}\chi\,(1 - \chi^2) \tag{59}$$

That should ensure — apart from significant loading changes — that once necklace coalescence has begun, internal necking does not activate until high c are reached.

6. Conclusion and perspectives

6.1. Conclusion

In this study, a yield criterion for porous anisotropic materials — Hill-type and single crystal — under axisymmetric loading has been developed using limit-analysis. In particular, it accounts for the transition from homogeneous yielding (void growth) to various inhomogeneous deformation modes: internal necking, columnar shielding and coalescence in columns. A strong effect of plastic anisotropy on strain localization modes, both in Hill materials and single crystals, is observed. When compared to the yield surface obtained through numerical limit analysis, a good agreement is obtained after limited calibration. In particular, the following findings about coalescence in columns, already made by Torki et al. (2023) for isotropic materials, are extended to anisotropic materials:

- coalescence in columns depends both on the axial ligament size c and the radial ligament size χ, as opposed to internal necking which only exhibits a variation with χ;
- depending on the microstructure and the plastic anisotropy, coalescence in columns can be favored over coalescence in layers over a significant range of loading conditions, including stress states with Lode angle $\theta = 0$ (hydrostatic tension superposed with uniaxial compression);
- contrary to internal necking, this deformation mode do not lead to complete loss of bearing capacity, which is confirmed by available experimental evidence (Benzerga et al., 2004a).

The occurrence of columnar shielding over a significant range of stress triaxialities is also predicted, which confirms previous numerical evidence (Chouksey et al., 2019).

Due to this clear physical grounding, the multi-surface plasticity model presented here outperforms the previous attempts to predict ductile fracture in anisotropic materials for axisymmetric loading conditions. In order to provide a complete homogenized model for porous Hill materials, the final yield surface was supplemented by a set of evolution laws for the microstructure so that the gradual process of ductile fracture can be simulated.

6.2. *Perspectives*

The perspectives are the following:

- In cases where the void axis and the main loading direction differ, equivalent voids could be defined using the method found in Torki and Benzerga (2018a) in order to use the expressions derived in this article, but this deserves additional validation.
- Yield surfaces for anisotropic materials can be extended to account for macroscopic shear which can lead to shear-assisted coalescence in layers. This would amount to adapt the work of Torki (2019) to anisotropic materials. It would also be interesting to study the effect of shear boundary conditions on columnar shielding and coalescence in columns, something that was not carried out in isotropic materials to begin with.
- Alternative evolutions laws could be obtained using continuous trial fields (*e.g.* the continuous field of Torki et al. (2023) for columnar localization and the internal necking field of Keralavarma and Chockalingam (2016) instead of the one of Benzerga and Leblond (2014) for layered localization). In any case, finite strain unit-cell simulations need to be conducted to assess definitively the quality of evolution laws.
- Once sound evolution laws are calibrated, it would be possible to study the effect of plastic anisotropy on material ductility, for instance by exploring failure loci for proportional loadings, *i.e.* fixed Lode angle and stress triaxiality (see Vishwakarma and Keralavarma (2019) for the corresponding study on isotropic materials). Such results would be of a paramount importance for the use of plastic anisotropy to design tougher materials.
- In single crystals, the issue of evolution laws is more complicated since strain inhomogeneities can have deeper consequences on plastic yielding. Indeed, even at the homogeneous yielding stage, Guo et al. (2020) has shown that local microstructure evolution can have significant effect on void growth at large strains; for instance, even if the macroscopic strain tensor has no shear terms, void shearing can occur due to local lattice rotation. The picture gets increasingly tangled when twinning occurs (Selvarajou et al., 2019; Indurkar et al., 2022). Therefore, in-depth investigation of these phenomena is required.

CRediT authorship contribution statement

Cédric Sénac: Conceptualization, Methodology, Software, Validation, Formal analysis, Data curation, Writing - original draft, Writing - review & editing, Visualization. **Jérémy Hure:** Methodology, Software, Writing - review & editing, Funding acquisition. **Benoît Tanguy:** Writing - review & editing, Funding acquisition.

Appendix A. Taylor surfaces of a porous single crystal

Deriving the tangent surface associated with the macroscopic potential given by Eq. 49 can be carried out following the lines of Section 3.1.2. It brings, for $\xi \neq 0$ and $\xi \neq \chi^2$:

$$\begin{aligned}\Sigma_{\rho\rho} &= \mathrm{sgn}(D_{33})\,\tau_0\left[\mathrm{sgn}(\xi-\chi^2)M_4(1-c) + M_2'(\xi)\mathcal{B}\left(\frac{\xi}{\sqrt{3}}\right) + \mathrm{sgn}(\xi)\left(\frac{M_2(\xi)+M_2'(\xi)\xi}{\sqrt{3}}\mathcal{A}\left(\frac{\xi}{\sqrt{3}}\right) + M_1\frac{w}{\sqrt{3}}\frac{(1-c)^2}{c}\right)\right] \\ \Sigma_{33}-\Sigma_{\rho\rho} &= \mathrm{sgn}(D_{33})\,\tau_0\left[-\mathrm{sgn}(\xi-\chi^2)M_4(1-c)\chi^2 - \mathrm{sgn}(\xi)\frac{\xi^2 M_2'(\xi)}{\sqrt{3}}\mathcal{A}\left(\frac{\xi}{\sqrt{3}}\right) + (M_2(\xi)-\xi M_2'(\xi))\,\mathcal{B}\left(\frac{\xi}{\sqrt{3}}\right)\right]\end{aligned} \tag{A.1}$$

whereas $\xi = 0$ results in:

$$\begin{aligned}\left|\Sigma_{\rho\rho} + \mathrm{sgn}(D_{33})\tau_0\left[(1-c)M_4 - (1-\chi^2)M_2'(0)\right]\right| &\leq \tau_0 M_1\frac{w}{\sqrt{3}}\frac{(1-c)^2}{c}\sqrt{\hat{h}_a} \\ \Sigma_{33}-\Sigma_{\rho\rho} &= \mathrm{sgn}(D_{33})\tau_0(1-c\chi^2)M_4\end{aligned} \tag{A.2}$$

and $\xi = \chi^2$ yields:

$$\begin{aligned}
&\left|\Sigma_{\rho\rho} - \mathrm{sgn}(D_{33})\tau_0 \left[\frac{M_2(\chi^2) + \chi^2 M_2'(\chi^2)}{\sqrt{3}} \mathcal{A}\left(\frac{\chi^2}{\sqrt{3}}\right) + M_2'(\chi^2)\mathcal{B}\left(\frac{\chi^2}{\sqrt{3}}\right) + M_1 \frac{w}{\sqrt{3}} \frac{(1-c)^2}{c}\right]\right| \leq \tau_0 M_4 (1-c) \\
&\Sigma_{33} - (1-\chi^2)\Sigma_{\rho\rho} = \mathrm{sgn}(D_{33})\tau_0 \left[\frac{M_2(\chi^2)}{\sqrt{3}} \chi^2 \mathcal{A}\left(\frac{\chi^2}{\sqrt{3}}\right) + M_2(\chi^2)\mathcal{B}\left(\frac{\chi^2}{\sqrt{3}}\right) + M_1 \frac{w}{\sqrt{3}} \frac{(1-c)^2}{c} \chi^2\right]
\end{aligned} \tag{A.3}$$

Similarly, the tangent surface associated with the macroscopic potential given by Eq. 50 can be obtained following the lines of Section 3.2.2, for $\xi \neq 0$ and $\xi \neq 1$:

$$\begin{aligned}
\Sigma_{33} - \Sigma_{\rho\rho} &= \mathrm{sgn}(D_{33})\,\tau_0 \left\{-\mathrm{sgn}(\xi - 1) M_4 (1-c) - \mathrm{sgn}(\xi) \frac{c}{\sqrt{3}} \left(\frac{\xi}{\bar{\xi}}\right)^2 M_2'\left(\frac{\xi}{\bar{\xi}}\right) \mathcal{A}\left(\frac{\xi}{\sqrt{3}\bar{\xi}}\right) + \mathrm{sgn}(\bar{\xi}) c \left[M_2\left(\frac{\xi}{\bar{\xi}}\right) - \frac{\xi}{\bar{\xi}} M_2'\left(\frac{\xi}{\bar{\xi}}\right)\right] \mathcal{B}\left(\frac{\xi}{\sqrt{3}\bar{\xi}}\right)\right\} \\
\Sigma_{33} &= \mathrm{sgn}(D_{33})\,\tau_0 \left\{\left[M_2\left(\frac{\xi}{\bar{\xi}}\right) + \left(1 - \frac{\xi}{\bar{\xi}}\right) M_2'\left(\frac{\xi}{\bar{\xi}}\right)\right]\left[\frac{\mathrm{sgn}(\xi)}{\sqrt{3}} \mathcal{A}\left(\frac{\xi}{\sqrt{3}\bar{\xi}}\right) + \mathrm{sgn}(\bar{\xi}) \mathcal{B}\left(\frac{\xi}{\sqrt{3}\bar{\xi}}\right)\right] + \mathrm{sgn}(\xi) M_1 \frac{\chi^3 - 3\chi + 2}{3\sqrt{3} w \chi}\right\}
\end{aligned} \tag{A.4}$$

The flat parts corresponding to $\xi = 0$ is:

$$\begin{aligned}
&\left|\Sigma_{\rho\rho} + \mathrm{sgn}(D_{33})\tau_0 \left[(1-c)\chi^2 M_4 - (1-\chi^2) M_2'(0)\right]\right| \leq \tau_0 M_1 \frac{\chi^3 - 3\chi + 2}{3\sqrt{3} w \chi} \\
&\Sigma_{33} - \Sigma_{\rho\rho} = \mathrm{sgn}(D_{33})\tau_0 (1 - c\chi^2) M_4
\end{aligned} \tag{A.5}$$

while $\xi = 1$ is associated to:

$$\begin{aligned}
&\left|\Sigma_{33} - \Sigma_{\rho\rho} - \mathrm{sgn}(D_{33}) c \tau_0 \left[-\frac{M_2'(1)}{\sqrt{3}} \mathcal{A}\left(\frac{1}{\sqrt{3}}\right) + (M_2(1) - M_2'(1))\, \mathcal{B}\left(\frac{1}{\sqrt{3}}\right)\right]\right| \leq \tau_0 (1-c) M_4 \\
&\Sigma_{33} = \mathrm{sgn}(D_{33})\tau_0 \left\{M_2(1)\left[\frac{1}{\sqrt{3}} \mathcal{A}\left(\frac{1}{\sqrt{3}}\right) + \mathcal{B}\left(\frac{1}{\sqrt{3}}\right)\right] + M_1 \frac{\chi^3 - 3\chi + 2}{3\sqrt{3} w \chi}\right\}
\end{aligned} \tag{A.6}$$

It is found that the coalescence stress established in Hure (2019) for internal necking is a special case of the result given above (Eq. A.6_b).

References

Barrioz, P., Hure, J., Tanguy, B., 2018. On void shape and distribution effects on void coalescence. Journal of Applied Mechanics 86, 011006.

Benzerga, A., 2000. Rupture ductile des tôles anisotropes. Ph.D. thesis. Ecole nationale supérieure des mines de Paris.

Benzerga, A., Besson, J., 2001. Plastic potentials for anisotropic porous solids. European Journal of Mechanics - A/Solids 20, 397–434.

Benzerga, A., Besson, J., Pineau, A., 2004a. Anisotropic ductile fracture: Part I - Experiments. Acta Materialia 52, 4623–4638.

Benzerga, A., Besson, J., Pineau, A., 2004b. Anisotropic ductile fracture: Part II - Theory. Acta Materialia 52, 4639–4650.

Benzerga, A.A., 2002. Micromechanics of coalescence in ductile fracture. Journal of the Mechanics and Physics of Solids 50, 1331–1362.

Benzerga, A.A., Leblond, J.B., 2010. Ductile fracture by void growth to coalescence. Advances in Applied Mechanics 44, 169–305.

Benzerga, A.A., Leblond, J.B., 2014. Effective yield criterion accounting for microvoid coalescence. J. Appl. Mech. 81.

Boyce, B.L., Clark, B.G., Lu, P., Carroll, J.D., Weinberger, C.R., 2013. The morphology of tensile failure in tantalum. Metallurgical and Materials Transactions A 44, 4567–4580.

Bramfitt, B.L., Marder, A.R., 1977. A study of the delamination behavior of a very low-carbon steel. Metallurgical Transactions A 8, 1263–1273.

CEA, 2022. Cast3m. www-cast3M.cea.fr .

Cheremskoy, P., Slezov, V., Betekhtin, V., 1990. Voids in solids. Energoatomizdat.

Chouksey, M., Basu, S., 2021. Exploration of subsequent yield surfaces through unit cell simulations. International Journal of Solids and Structures 219-220, 11–22.

Chouksey, M., Keralavarma, S.M., Basu, S., 2019. Computational investigation into the role of localisation on yield of a porous ductile solid. Journal of the Mechanics and Physics of Solids 130, 141–164.

Chouksey, M., Keralavarma, S.M., Basu, S., 2020. Exploring subtle features of yield surfaces of porous, ductile solids through unit cell simulations. Mechanics of Materials 151, 103605.

Gologanu, M., Leblond, J.B., 1997. Recent extention of Gurson's model for porous ductile metals. Continuum micromechanics 377, 61–130.

Gologanu, M., Leblond, J.B., Perrin, G., Devaux, J., 2001. Theoretical models for void coalescence in porous ductile solids - i. Coalescence "in layers". International Journal of Solids and Structures 38, 5581–5594.

Guo, H.J., Ling, C., Busso, E.P., Zhong, Z., Li, D.F., 2020. Crystal plasticity based investigation of micro-void evolution under multi-axial loading conditions. International Journal of Plasticity 129, 102673.

Gurson, A., 1977. Continuum theory of ductile rupture by void nucleation and growth: Part I - Yield criteria and flow rules for porous ductile media. Journal of Engineering Materials and Technology 99, 2–15.

Han, X., Besson, J., Forest, S., Tanguy, B., Bugat, S., 2013. A yield function for single crystals containing voids. International Journal of Solids and Structures 50, 2115–2131.

Hill, R., 1948. A theory of the yielding and plastic flow of anisotropic metals. Proc. R. Soc. Lond. A 193, 281–297.

Hosseini, N., Nieto-Fuentes, J., Dakshinamurthy, M., Rodríguez-Martínez, J., Vadillo, G., 2022. The effect of material orientation on void growth. International Journal of Plasticity 148, 103149.

Hure, J., 2019. A coalescence criterion for porous single crystals. Journal of the Mechanics and Physics of Solids 124, 505–525.

Hure, J., Barrioz, P.O., 2016. Theoretical estimates for flat voids coalescence by internal necking. Eur. J. Mech. A/Solids 60, 217–226.

Hutchinson, J.W., 1976. Bounds and self-consistent estimates for creep of polycrystalline materials. Proceedings of the Royal Society of London A 348, 101–127.

Indurkar, P.P., Joshi, S.P., Benzerga, A.A., 2022. On the micromechanics of void mediated failure in hcp crystals. Journal of the Mechanics and Physics of Solids 165, 104923.

Keralavarma, S., Chockalingam, S., 2016. A criterion for void coalescence in anisotropic ductile materials. International Journal of Plasticity 82, 159–176.

Keralavarma, S., Hoelscher, S., Benzerga, A., 2011. Void growth and coalescence in anisotropic plastic solids. International Journal of Solids and Structures 48, 1696–1710.

Keralavarma, S., Reddi, D., Benzerga, A., 2020. Ductile failure as a constitutive instability in porous plastic solids. Journal of the Mechanics and Physics of Solids 139, 103917.

Keralavarma, S.M., 2017. A multi-surface plasticity model for ductile fracture simulations. Journal of the Mechanics and Physics of Solids 103, 100–120.

Keralavarma, S.M., Benzerga, A.A., 2010. A constitutive model for plastically anisotropic solids with non-spherical voids. Journal of the Mechanics and Physics of Solids 58, 874–901.

Koiter, W.T., 1953. Stress-strain relations, uniqueness and variational theorems for elastic-plastic materials with a singular yield surface. Quarterly of Applied Mathematics 11, 350–354.

Leblond, J.B., Kondo, D., Morin, L., Remmal, A., 2018. Classical and sequential limit analysis revisited. Comptes Rendus Mécanique 346, 336–349.

Leblond, J.B., Morin, L., 2014. Gurson's criterion and its derivation revisited. Journal of Applied Mechanics 81, 51012.

Ling, C., Besson, J., Forest, S., Tanguy, B., Latourte, F., Bosso, E., 2016. An elastoviscoplastic model for porous single crystals at finite strains and its assessment based on unit cell simulations. International Journal of Plasticity 84, 58–87.

Madou, K., Leblond, J.B., 2012a. A Gurson-type criterion for porous ductile solids containing arbitrary ellipsoidal voids I : Limit-analysis of some representative cell. Journal of the Mechanics and Physics of Solids 60, 1020–1036.

Madou, K., Leblond, J.B., 2012b. A gurson-type criterion for porous ductile solids containing arbitrary ellipsoidal voids—ii: Determination of yield criterion parameters. Journal of the Mechanics and Physics of Solids 60, 1037–1058.

Mbiakop, A., Constantinescu, A., Danas, K., 2015. An analytical model for porous single cristals with ellipsoidal voids. Journal of the Mechanics and Physics of Solids 84, 436–467.

Monchiet, V., Cazacu, O., Charkaluk, E., Kondo, D., 2008. Macroscopic yield criteria for plastic anisotropic materials containing spheroidal voids. International Journal of Plasticity 24, 1158–1189.

Morin, L., 2012. Influence de l'effet de forme et de taille des cavités, et de l'anisotropie plastique sur la rupture ductile. Ph.D. thesis. Université Pierre et Marie Curie.

Morin, L., Leblond, J.B., Benzerga, A.A., 2015a. Coalescence of voids by internal necking : Theoretical estimates and numerical results. Journal of the Mechanics and Physics of Solids 75, 140–158.

Morin, L., Leblond, J.B., Benzerga, A.A., Kondo, D., 2016a. A unified criterion for the growth and coalescence of microvoids. Journal of the Mechanics and Physics of Solids 97, 19–36.

Morin, L., Leblond, J.B., Kondo, D., 2015b. A Gurson-type criterion for plastically anisotropic solids containing arbitrary ellipsoidal voids. International Journal of Solids and Structures 77, 86–101.

Morin, L., Leblond, J.B., Tvergaard, V., 2016b. Application of a model of plastic porous materials including void shape effects to the prediction of ductile failure under shear-dominated loadings. Journal of the Mechanics and Physics of Solids 94, 148–166.

Nemat-Nasser, S., Hori, M., 1993. Micromechanics: Overall properties of heterogeneous materials. Elsevier.

Pala, R., Dzioba, I., 2018. Influence of delamination on the parameters of triaxial state of stress before the front of the main crack. AIP Conference Proceedings 2029. URL: https://doi.org/10.1063/1.5066514, doi:10.1063/1.5066514, arXiv:https://pubs.aip.org/aip/acp/article-pdf/doi/10.1063/1.5066514/13798800/020052_1_online.pdf. 020052.

Pardoen, T., 1998. Ductile fracture of cold-drawn copper bars: Experimental investigation and micromechanical modeling. Ph.D. thesis. Université Catholique de Louvain.

Pardoen, T., Hutchinson, J., 2000. An extended model for void growth and coalescence. Journal of the Mechanics and Physics of Solids 48, 2467–2512.

Paux, J., Morin, L., Brenner, R., Kondo, D., 2015. An approximate yield criterion for porous single crystals. European Journal of Mechanics A/Solids 51, 1–10.

Pineau, A., Benzerga, A., Pardoen, T., 2016. Failure of metals: Part I - Brittle and ductile fracture. Acta Materiala 107, 424–483.

Reddi, D., Areej, V., Keralavarma, S., 2019. Ductile failure simulations using a multi-surface coupled damage-plasticity model. International Journal of Plasticity 118, 190–214.

Requena, G., Maire, E., Leguen, C., Thuillier, S., 2014. Separation of nucleation and growth of voids during tensile deformation of a dual phase steel using synchrotron microtomography. Materials Science and Engineering: A 589, 242–251. URL: https://www.sciencedirect.com/science/article/pii/S0921509313010691, doi:https://doi.org/10.1016/j.msea.2013.09.084.

Rice, J.R., Tracey, D.M., 1969. On the ductile enlargement of voids in triaxial stress fields. Journal of the Mechanics and Physics of Solids 17, 201–217.

Rodriguez, A., Mansoor, B., Ayoub, G., Colin, X., Benzerga, A., 2020. Effect of uv-aging on the mechanical and fracture behavior of low density polyethylene. Polymer Degradation and Stability 180, 109185. URL: https://www.sciencedirect.com/science/article/pii/S0141391020301178, doi:https://doi.org/10.1016/j.polymdegradstab.2020.109185.

Saeidi, N., Ashrafizadeh, F., Niroumand, B., Forouzan, M.R., Barlat, F., 2015. Influence of bainite morphology on ductile fracture behavior in a 0.C-CrMoNi steel. Steel Research International 86, 528–535. URL: https://onlinelibrary.wiley.com/doi/abs/10.1002/srin.201400155, doi:https://doi.org/10.1002/srin.201400155, arXiv:https://onlinelibrary.wiley.com/doi/pdf/10.1002/srin.201400155.

Salençon, J., 1983. Calcul à la rupture et analyse limite. Presses de l'école nationale des Ponts et chaussées.

Scherer, J.M., Besson, J., Forest, S., Hure, J., Tanguy, B., 2021. A strain gradient plasticity model of porous single crystal ductile fracture. Journal of the Mechanics and Physics of Solids 156, 104606.

Selvarajou, B., Joshi, S., Benzerga, A., 2019. Void growth and coalescence in hexagonal close packed crystals. Journal of the Mechanics and Physics of Solids 125, 198–224.

Seo, D., Toda, H., Kobayashi, M., Uesugi, K., Takeuchi, A., Suzuki, Y., 2015. In situ observation of void nucleation and growth in a steel using X-ray tomography. ISIJ International 55, 1474–1482. doi:10.2355/isijinternational.55.1474.

Suquet, P., 1982. Plasticité et homogénéisation. Ph.D. thesis. Université Pierre et Marie Curie.

Sénac, C., Hure, J., Tanguy, B., 2023. Void growth yield criteria for intergranular ductile fracture. Journal of the Mechanics and Physics of Solids 172, 105167.

Sénac, C., Scherer, J.M., Hure, J., Helfer, T., Tanguy, B., 2022. Homogenized constitutive equations for porous single crystals plasticity. European Journal of Mechanics - A/Solids , 104642.

Taylor, G., 1938. Plastic strains in metals. J. Inst. Metals 62, 307–324.

Tekoǧlu, C., Leblond, J.B., Pardoen, T., 2012. A criterion for the onset of void coalescence under combined tension and shear. Journal of the Mechanics and Physics of Solids 60, 1363–1381.

Thomason, P.F., 1985. Three-dimensional models for the plastic limit-loads at incipient failure of the intervoid matrix in ductile porous solids. Acta Metallurgica 33, 1079–1085.

Torki, M., Benzerga, A., Leblond, J.B., 2015. On void coalescence under combined tension and shear. Journal of Applied Mechanics 82, 071005.

Torki, M., Benzerga, A.A., 2022. Ductile Fracture in Plane Stress. Journal of Applied Mechanics 89.

Torki, M., Keralavarma, S., Benzerga, A., 2021. An analysis of Lode effects in ductile failure. Journal of the Mechanics and Physics of Solids 153, 104468.

Torki, M., Medrano, F., Benzerga, A., Leblond, J.B., 2023. A model of void coalescence in columns. Journal of the Mechanics and Physics of Solids 171, 105134.

Torki, M., Tekog lu, C., Leblond, J.B., Benzerga, A., 2017. Theoretical and numerical analysis of void coalescence in porous ductile solids under arbitrary loadings. International Journal of Plasticity 91, 160–181.

Torki, M.E., 2019. A unified criterion for void growth and coalescence under combined tension and shear. International Journal of Plasticity 119, 57–84.

Torki, M.E., Benzerga, A.A., 2018a. A mechanism of failure in shear bands. Extreme Mechanics Letters 23, 67–71.

Torki, M.E., Benzerga, A.A., 2018b. Micromechanics-based constitutive relations for post-localization analysis. MethodsX 5, 1431–1439.

Van Houtte, P., 1988. A comprehensive mathematical formulation of an extended Taylor–Bishop–Hill model featuring relaxed constraints, the Renouard–Wintenberger theory and a strain rate sensitivity model. Texture, Stress, and Microstructure 8, 313–350.

Vishwakarma, V., Keralavarma, S., 2019. Micromechanical modeling and simulation of the loading path dependence of ductile failure by void growth and coalescence. International Journal of Solids and Structures 166, 135–153.

Wang, H., Tian, Y., Ye, Q., Wang, Q., Wang, Z., Wang, G., 2022. Effect of delamination on ductile fracture during the impact test in ultra-heavy steel. Journal of Materials Engineering and Performance 31, 7843–7855.

Yerra, S., Tekoğlu, C., Scheyvaerts, F., Delannay, L., Houtte, P.V., Pardoen, T., 2010. Void growth and coalescence in single crystals. International Journal of Solids and Structures 47, 1016–1029.